

Interpretable machine learning for high-dimensional trajectories of aging health

Spencer Farrell,^{1,*} Arnold Mitnitski,² Kenneth Rockwood,² and Andrew Rutenberg^{1,†}

¹*Department of Physics and Atmospheric Science,
Dalhousie University, Halifax, Nova Scotia, Canada*

²*Division of Geriatric Medicine, Dalhousie University, Halifax, Nova Scotia, Canada*

(Dated: May 10, 2021)

We have built a computational model for individual aging trajectories of health and survival, which contains physical, functional, and biological variables, and is conditioned on demographic, lifestyle, and medical background information. We combine techniques of modern machine learning with an interpretable interaction network, where health variables are coupled by explicit pair-wise interactions within a stochastic dynamical system. Our model is scalable to large longitudinal data sets, is predictive of individual high-dimensional health trajectories and survival from baseline health states, and infers an interpretable network of directed interactions between the health variables. The network identifies plausible physiological connections between health variables and clusters of strongly connected health variables. We use English Longitudinal Study of Aging (ELSA) data to train our model and show that it performs better than dedicated linear models for health outcomes and survival. Our model can also be used to generate synthetic individuals that age realistically, to impute missing data, and to simulate future aging outcomes given arbitrary initial health states.

I. INTRODUCTION

Aging is a high-dimensional process due to the enormous number of aspects of healthy functioning that can change with age across a multitude of physical scales [1, 2]. This complexity is compounded by the heterogeneity and stochasticity of individual aging outcomes [3, 4]. Strategies to simplify the complexity of aging include identifying key biomarkers that quantitatively assess the aging process [5, 6] or integrating many variables into simple and interpretable one-dimensional summary measures of the progression of aging, as with “Biological Age” [7–9], clinical measures such as frailty [10, 11], or recent machine learning models of aging [12, 13]. Nevertheless, one-dimensional measures only summarize the progression of aging, and so can miss significant aspects of high-dimensional aging trajectories and of heterogeneous aging outcomes. We introduce a machine learning approach to model high-dimensional trajectories directly, while still learning interpretable aspects of our model through an explicit network of interactions between variables.

The increasing availability of large longitudinal aging studies is beginning to provide the rich data-sets necessary for the development of flexible machine learning models of aging [14]. Methods for predictive modelling of individual health trajectories of disease progression have already been developed [15–20], but they generally are not joint models that include both mortality and the progression of aging [20]. There has also been progress on learning interpretable summaries of aging progression [12, 13], generalizing biological-age approaches but still producing low-dimensional summaries of aging.

Less progress has been made on the more general problem of modeling high-dimensional aging trajectories. Stochastic-process joint models that simultaneously

model longitudinal and survival data have been proposed [21–23], but have only been implemented for one or two health variables at a time. Farrell *et al.* [24] used cross-sectional data to build a network model that generated trajectories of 10 health variables and predicted survival, but it was limited to binary health measures.

In this work we use the English Longitudinal Study of Aging (ELSA, [25]), which is a large observational population study including a wide variety of variables with follow-up measurements for up to 20 years including mortality. Like other large observational studies, for most individuals it has many missing measurements, few irregularly-timed follow-ups, and censored mortality. Any practical approach to model such data must confront the challenges provided by missing and irregularly timed data and mortality censoring.

While machine learning (ML) approaches can help us navigate these challenges with available data, they face additional challenges of interpretability [14, 26]. “Scientific Machine Learning” [27] or “Theory guided data science” [28] suggests that domain knowledge be used to constrain and add interpretability to ML models. For example, we can require that aging is modelled as a network of interacting health components [29, 30], and that stochastic differential equations (SDEs) model the dynamical evolution of high-dimensional health states [21]. On the other hand we can use general ML approaches to model survival, where we may not be interested in interpretation, or to impute missing data for baseline (initial) health states.

The result (see Fig. 1) is a powerful and flexible, but interpretable, approach to modelling aging and mortality from high-dimensional longitudinal data – one that preserves but is not crippled by the complexity of aging. We evaluate the resulting model with test data and compare with simpler linear modelling approaches. We use a Bayesian approach to infer the posterior distribution of the both interaction network and individual health trajectories to estimate confidence bounds. We demonstrate our model’s ability to robustly predict health trajectories

* spencer.farrell@dal.ca

† adr@dal.ca

using an interpretable network of interactions.

II. RESULTS

ELSA dataset. We combine waves 0 to 8 in the English Longitudinal Study of Aging (ELSA, [25]) to build a dataset of $M = 25290$ individuals, with longitudinal follow-up of up to 20 years. In this study, self-reported health information is obtained approximately every 2 years and nurse-evaluated health with physical assessment and blood tests approximately every 4 years. Considering all waves together with 2 year increments, 27% of values are missing for self-reported variables, 78% of values are missing for nurse-evaluated variables, and 96% of individual mortality is censored.

An individual’s health state is observed at K times $\{t_k\}_{k=1}^K$ with a set of health variables $\{\mathbf{y}_{t_k}\}_{k=1}^K$. The vectors \mathbf{y}_{t_k} describe the N -dimensional health state of an individual, where each of the N dimensions represents a separate health measurement. We select $N = 29$ continuous-valued or discrete ordinal variables that were measured for at least two of the waves. Individuals also have background (demographic, diagnostic, or lifestyle) information observed at baseline, which is described by an B -dimensional vector \mathbf{u}_{t_0} . We select $B = 19$ of these continuous or discrete valued background variables. Variables used from the data-set were selected only by availability, not by predictive quality. All chosen variables and the number of observed individuals for each is shown in Supplemental Fig. 1, the details of the variables are given in Supplemental Table 1.

DJIN model of aging. We build a model to forecast an individual’s future health $\{\mathbf{y}_{t_k}\}_{k>0}$ and survival probability $\{S(t_k)\}_{k>0}$ given their baseline age t_0 , baseline health \mathbf{y}_{t_0} and background health variables \mathbf{u}_{t_0} . It is a dynamic, joint, interpretable network (DJIN) model of aging. A schematic of our model is shown in Fig. 1, while mathematical details are provided in the Methods.

Fig. 1a illustrates our method of imputation for the baseline health state. Effective imputation is essential because none of the 25290 individuals in the data-set have a fully observed baseline health state. Variational auto-encoders have shown promising results for imputation [31, 32]. We impute with a normalizing-flow variational auto-encoder [33], where a neural network (green trapezoid) encodes the known information about the individual into an individual-specific latent distribution, and a second neural network (orange trapezoid) is used to decode states sampled from the latent distribution into imputed values. This is a multiple imputation process that outputs samples from a distribution of imputed values rather than a single estimate.

Fig. 1b illustrates our method of generating synthetic baseline health states given only background health information, which is an alternative method of sampling totally synthetic baseline health states. We randomly

sample the prior population distribution of the latent space used in imputation, and then combine this with arbitrary background information and use the same decoder as in imputation to generate a synthetic baseline health state. With repeated random samples of the latent space we generate a distribution of synthetic baseline health states.

Fig. 1c illustrates the temporal dynamics of the model. Dynamics start with the imputed or generated baseline state \mathbf{x}_0 . The health state is then evolved in time with a set of stochastic differential equations, similar to the Stochastic Process Model of Yashin *et al.* [21, 22, 34, 35]. The stochastic dynamics capture the inherent stochasticity of the aging process. We assume linear interactions between the variables, with an interpretable interaction network \mathbf{W} .

Fig. 1d illustrates the mortality component of the model. The temporal dynamics of the health state is fed into a recurrent neural network (RNN) to estimate the individual hazard rate for mortality, and to compute an individual survival function. Recent work shows that this approach can work well in joint models [20]. The RNN architecture lets us use the history of previous health states in mortality (a non-RNN version of the model is summarized in Supplemental Fig. 12).

We use a Bayesian approach to model uncertainty by estimating the posterior distribution of parameters, of health trajectories and of survival curves – as illustrated by the shaded blue confidence intervals in Fig. 1C. To handle our large and high-dimensional datasets, we use a variational approximation to the posterior [36] instead of slower MCMC methods. The variational approximation reduces the sampling problem to an optimization problem, which we can efficiently approach using stochastic gradient descent. Mathematical details are provided in the Methods. The code for our model is available at <https://github.com/Spencerfar/djin-aging>.

Validation of model survival trajectories. We evaluate our model with test individuals withheld from training. Given baseline age t_0 , baseline health variables \mathbf{y}_{t_0} , and background information \mathbf{u}_{t_0} for each of these test individuals, we impute missing baseline variables and predict future health trajectories and mortality with the model. These predictions are compared with their observed values.

The C-index measures the model’s ability to discriminate between individuals at high or low risk of death. We use a time-dependent C-index [37], which is the proportion of distinct pairs of individuals where the model correctly predicts that individuals who died earlier had a lower survival probability. Higher scores are better; random predictions give 0.5. In Fig. 2a we see that our model (red circles) performs substantially better than a standard Cox proportional hazards model (green squares) with elastic net regularization and random forest MICE imputation [38, 39]. The horizontal lines show the C-index scores for the entire test set, and the points show

predictions stratified by baseline age. Stratification allows us to remove age-effects in the predictions, so we can determine how well the model uses health variables to discriminate between pairs of individuals at the same age. Our model predictions do not substantially degrade when controlling for age, indicating that it is learning directly from health variables, rather than from age. DJIN predictions do degrade at older baseline ages due to the limited sample size.

We evaluate the detailed accuracy of survival curve predictions with the Brier score [40]. Individual Brier scores calculate squared error between the full predicted survival distribution $S(t)$ and the exact survival “distribution” for that individual, which is a step-function equal to 1 when the individual is alive and 0 when they are dead. Lower Brier scores are better. In Fig. 2b we show the average Brier score for different death ages for our model (blue) and a Cox model with a Breslow baseline hazard (green), indicating our model has a substantially lower error between the predicted and exact survival distributions for older ages (note the log-scale). The Integrated Brier Score (IBS) is computed by integrating these curves over the range of observed death ages, and highlights the improvement of predictive accuracy of our model as compared to Cox.

We evaluate the calibration of survival predictions with the D-calibration score [41]. For a well-calibrated survival curve prediction, half of the test individuals should die before their predicted median death age and half should live longer. Calibrated survival probabilities allow them to be interpreted as an estimate of absolute risk rather than relative risk. The D-calibration score generalizes this to more quantiles of the survival curve, where the proportion observed in each predicted quantile should be uniformly distributed. In Fig. 2c, we show deciles of the survival probability for our model (red bins), compared with the expected uniform black straight line. We compute χ^2 statistics and p-values for the predictions of our model vs the uniform ideal, as well as for a Cox proportional hazards model (histogram in Supplemental Fig. 13). Our model is consistent with a uniform distribution under this test ($p = 1.0$, $\chi^2 = 1.3$) as desired for calibrated probabilities. The Cox model is also calibrated ($p = 1.0$, $\chi^2 = 2.1$), but with a slightly worse χ^2 statistic.

These results demonstrate that our DJIN model accurately predicts the relative risk of mortality of individuals (assessed by the C-index), predicts accurate survival probabilities (assessed by the Brier score), and properly calibrates these survival probabilities so that they can be directly interpreted as an absolute risk of death rather than only as a relative risk.

Validation of model health trajectories. Model predictions of individual health trajectories are also evaluated on the test set. We compute the Root-Mean-Square Error (RMSE) for each health variable, and create a relative RMSE score by dividing by the RMSE obtained

when using the age and sex matched training-set population mean as the prediction. In Fig. 2d, we show that the model (red circles) performs better than the age and sex dependent population mean (black dashed line) when the baseline value of the particular variable is observed. The RMSE here is computed for all predictions between 1 and 6 years from baseline. In Fig. 2e we show that the model is predictive of future health values even when the initial value of the particular variable is imputed.

As measured by the relative RMSE, our model is better than a null model (blue squares) that carries forward the observed baseline (d) or imputed baseline value (e) for all ages. For comparison purposes, we also developed a linear model with elastic net regularization and random-forest MICE imputation [38, 39] that has been trained separately to predict each health variable. We are comparing our single DJIN model that predicts all 29 variables, to 29 independently-trained linear models. While the linear models perform better than the null model for observed baselines, our model performs better than both. For imputed baselines, the linear model with random-forest MICE imputation performs poorly even compared to the imputed null model, while our model continues to outperform both.

In Fig. 2f, we show boxplots of RMSE scores over the health variables for 1-14 years past baseline, when the variable was initially observed at baseline. The model is predictive for even long term predictions, and remains better than linear elastic net predictions for at least 14 years past baseline for the self-report waves (blue) and 12 years past baseline for the nurse waves including blood biomarkers (pink).

In Supplemental Fig. 3 we show example DJIN trajectories for 3 individuals in the test set for the 6 best predicted health variables. We show both the mean predicted model trajectory and a visualization of the uncertainty in the trajectory. For comparison, the population mean and elastic net linear model are shown. The predicted trajectories visually agree well with the data, and is often substantially better than either the elastic net linear predictions or the population means for the corresponding variables.

These results demonstrate that our DJIN model predicts the values of future health variables from baseline better than standard linear models, and better than population-mean or constant baseline models.

Validation of generated synthetic populations. Given baseline age t_0 , and background information \mathbf{u}_{t_0} for test individuals, we generate synthetic baseline health states and simulate a corresponding synthetic aging population. We evaluate these aging trajectories by comparing with the observed test population. We train a logistic regression classifier to evaluate if the synthetic and observed populations can be distinguished [18, 19, 42, 43]. We find that this classifier has below a 57% accuracy for the first 14 years past baseline (Supplemental Fig. 5) – only slightly better than random.

In Supplemental Figs. 6 and 7 we show the population and synthetic baseline distributions and population summary statistics for the trajectories vs age for ages 65 to 90. We find that our model captures the mean of the population, but tends to underestimate the standard deviation of the population (as expected [36]). In Supplemental Fig. 4 we show the population synthetic survival function agrees with the observed population survival below age 90, where the majority of data lies.

The agreement of the synthetic and test populations demonstrates the DJIN model’s ability to generate a synthetic population of aging individuals that resemble the observed population, though with less variation.

DJIN infers interpretable sparse interaction networks. Our Bayesian approach infers the approximate posterior distribution of the interaction network weights; Fig. 3 visualizes the network with the mean posterior weights. Weights with a 99% posterior credible interval including zero have been pruned (white) – all visible weights have posterior credible intervals either fully above or fully below zero. This cutoff is demonstrated in Supplemental Fig. 9.

Connections are read as starting at the variable on the horizontal axis (j), and ending at the variable on the vertical axis (i), representing the connection weight matrix $W_{i \leftarrow j}$. Positive connections indicate that an increasing variable j influences an increase in variable i . Negative connections mean an increasing variable j influences a decrease in variable i . The interaction network is sparse, with typically only a small number of inferred interactions for each health variable.

This inferred causal network can be readily and directly interpreted. For example, we see strong connections between Vitamin-D and self-rated health, between ADL score and walking ability, and between glucose and glycated hemoglobin. The sign of the connections indicates the direction of influence. For example, a decrease in gait speed influences an increase in self-reported health score (worse health), an increase in the time required to complete chair rises, and a decrease in grip strength.

Hierarchical clustering on the connection weights is indicated in Fig. 3, and the ordering of the variables in the heatmap represents this hierarchy. Many of these inferred clusters of nodes plausibly fit with known physiology. For example, most blood biomarker measurements (bottom half) are separated from the physical/functional measurements (top half, purple cluster). Other inferred clusters include blood pressure and pulse (orange) and lipids (green).

III. DISCUSSION

We have developed a machine learning aging model, DJIN, to predict both multidimensional health trajectories and survival given baseline information, and to generate realistic synthetic aging populations – while also

learning interpretable network interactions that characterize the dynamics. The DJIN model uses continuous-valued health variables from the ELSA dataset, including physical, functional, and molecular variables. We have shown that the comprehensive DJIN model performs better than 30 independent regularized linear models that were trained specifically for each separate health variable or survival prediction task.

While summary measures of aging such as the frailty index or biological age are easily interpretable, they are only one-dimensional – we find that the changes that occur due to aging are multidimensional. We show in Supplemental Fig. 10 that a one-dimensional measure cannot predict individual aging health trajectories as well as our multidimensional DJIN model. This is because all individuals do not age along the same trajectory.

Previously, we had built a weighted network model (WNM) using cross-sectional data with only binary health deficits [24]. That WNM did not incorporate continuous health variables and could not be efficiently trained with longitudinal data. As a result, the networks inferred by that model were not robust – and resulted in many qualitatively distinct networks that were consistent with the observed cross-sectional binary data. In contrast, the DJIN model uses many continuous valued health variables and can be efficiently trained with large longitudinal datasets. As a result, the DJIN model produces a robust and interpretable interaction network of multidimensional aging.

Recently, other machine learning models of aging or aging-related disease progression have been emerging [12, 18–20, 43]. Since they each differ significantly in terms of both the datasets, types of data used, and scientific goals, it is still too early to see which approaches are best – and for which data and what goals. We use ELSA data since it is longitudinal (to facilitate modelling trajectories), has many continuous variables (to allow modelling of continuous trajectories and constructing an interaction network that is at the core of our model), and includes mortality (to develop our joint mortality model). The ELSA data is representative of many large-scale aging data sets.

Our scientific goals were to obtain good predictive accuracy from baseline for both health trajectories and mortality, while at the same time obtaining an interpretable network of interactions between health variables [14]. To achieve these goals with the ELSA data, we had to do significant imputation to complete the baseline states. We include stochastic dynamics within a Bayesian model framework to obtain uncertainties for both our predictions and the interaction network. The Bayesian approach is computationally intensive and necessitated a variational approximation to the posterior that tends to underestimate uncertainty [36]. From the analysis of synthetic populations (see Supplemental Figs. 4, 6, and 7), this underestimate appears to be modest.

The DJIN model is not computationally demanding, needing only approximately 12 hours to run with 1 GPU

for $M = 25290$ individuals, $B = 19$ baseline variables, $N = 29$ health-variables, and up to $K = 20$ years of longitudinal data. We expect better performance and generalizability with more individuals M . Because of the interactions between health variables we also expect better performance with more health variables N . We note that binary health variables, or mixtures of binary and continuous variables, could be used with only small adjustments. Since computational demands for a forward pass of the model scale approximately linearly with M and K , and quadratically with $B + N$, our existing DJIN model is already practical for significantly larger datasets.

In this work we only consider predictions from the baseline state at a single age. We anticipate that individual prediction could be significantly improved by utilizing more than one input time to impute the baseline health state \mathbf{x}_0 or by conditioning the predictions on multiple input ages. This can be done using a recurrent neural network [44, 45]. Observed time-points after baseline can also be used to update the dynamics [46] for predictions of continually observed individuals in personalized medicine applications. However, both of these developments would either require data with more follow-up times than we had available, or limiting predictions to very short time intervals. For these reasons, we chose to model trajectories using only the baseline health state.

We developed an imputation method that is trained along with the longitudinal dynamics to impute missing baseline data. This imputation method can also be used to generate synthetic individuals conditioned on baseline demographic information. Large synthetic datasets can facilitate the development of future models and techniques by providing high-quality training data [47], and are especially needed given the lack of large longitudinal studies of aging [14]. In Supplemental Figs. 4, 5, 6, and 7 we show that our synthetic population is comparable to the available individuals in the ELSA dataset. We have also provided a synthetic population of nearly 10^7 individuals with annually sampled trajectories from baseline for 20 years [48].

At the heart of our dynamical model is a directed and signed network that is directly interpretable. The DJIN model does not just make “black-box” predictions, but is learning a plausible physiological model for the dynamics of the health variables. The network is not a correlation/association network (see comparison in Supplemental Fig. 8) [8, 49, 50], but instead determines how the current value of the health variables influence future changes to connected health variables, leading to coupled dynamics of the health variables. This establishes a predictive link between variables [51]. Similar directed linear networks are inferred in neuroscience with Dynamic Causal Modelling [52, 53]. When interpreting the magnitude of weights, links function as in standard regression models: weight magnitudes will be dependent on the variables included in the model, and can decrease if stronger predictor variables are added. Given the efficiency of our

computational approach, including more variables is recommended if they are available.

The directed nature of the network connections lend themselves to clinical interpretation – for example that that ADL impairment has an effect on IADL impairment and not vice versa, and that both have an effect on general function score and vice versa. The directed network of interactions suggests avenues to explore for interventions. For a given intervention (for example drug, exercise, or diet) we can ascertain which effects of the intervention are beneficial and which are deleterious. In principle, we could also predict the outcome of multiple interventions such as in polypharmacy [54]. A similar approach could be taken for chronic diseases or disorders. These avenues will be increasingly feasible and desirable with longitudinal ‘omics data-sets, where the interactions are not already largely determined by previous work.

We caution that our model does not currently take into account how interventions may change relationships over time, or any higher order interactions than the pair-wise interactions considered here. For example, the interaction between sodium levels, mobility, and diuretics appears to be strong [55], but would not be captured in our current model. Extending our approach to include such effects in the interactions would be desirable.

The accuracy of our model can be slightly improved if a network interpretation of the dynamics is not desired – for instance if the goal is only prediction. In Supplemental Fig. 11, we show that using a neural network instead of pair-wise network interactions somewhat improves health variable prediction accuracy for a handful of variables. However, our goal was to demonstrate both good predictions *and* interpretability. The network form of our dynamics can be replaced with any alternative model of the aging dynamics for bespoke interpretability.

The advantage of more interpretable models will be more clearly seen when multiple data-sets are compared – since interpretability facilitates comparisons between cohorts, groups, or even between model organisms. Every aspect of our DIJN model can be made more structured, explicit and “interpretable”. For example, proportional hazards [56] or quadratic hazards [21] could be used for mortality. While this would reduce performance compared to our more general neural network, it would add interpretability to the survival predictions.

Our work opens the door to many possible follow-up studies. Our DJIN model can be applied to any organism or set of variables that has enough individual longitudinal measurements. With genomic characterization of populations, the background health information \mathbf{u}_{t_0} can be greatly expanded to examine the intrinsic variability of aging [3, 4] and mortality determined by genetic variation. By including genomic, lab-test, and functional data we could use the interpretable interactions to determine how different organismal scales of health data interact in determining human aging trajectories. By including drug and behavioral (exercise, diet) interven-

tions as background variables, we can better determine how they affect health during aging. Finally, large longitudinal multi-omics datasets [57, 58] could be used to build integrative models of human health.

We have demonstrated a viable interpretable machine learning (ML) approach to build a model of human aging with a large longitudinal study. The future of these

approaches is bright [14], since we are only starting to embrace the complexity of aging with large longitudinal datasets. While ML models can find immediate application in understanding patterns of aging health in populations, we foresee that similar techniques will eventually reach into clinical practice to guide personalized medicine of aging health.

-
- [1] T. B. L. Kirkwood, *Cell* **120**, 437 (2005).
- [2] C. López-Otín, M. A. Blasco, L. Partridge, M. Serrano, and G. Kroemer, *Cell* **153**, 1194 (2013).
- [3] L. A. Herndon, P. J. Schmeissner, J. M. Dudaronek, P. A. Brown, K. M. Listner, Y. Sakano, M. C. Paupard, D. H. Hall, and M. Driscoll, *Nature* **419**, 808 (2002).
- [4] T. B. L. Kirkwood and C. E. Finch, *Nature* **419**, 794 (2002).
- [5] A. E. Kane and D. A. Sinclair, *Mechanisms of Ageing and Development* **180**, 117 (2019).
- [6] L. Ferrucci, M. Gonzalez-Freire, E. Fabbri, E. Simon-sick, T. Tanaka, Z. Moore, S. Salimi, F. Sierra, and R. de Cabo, *Aging Cell* **19**, e13080 (2020).
- [7] M. E. Levine, *The Journals of Gerontology: Series A* **68**, 667 (2012).
- [8] A. B. Mitnitski, J. E. Graham, A. J. Mogilner, and K. Rockwood, *BMC Geriatrics* **2**, 1 (2002).
- [9] S. Horvath, *Genome Biology* **14**, R115 (2013).
- [10] A. B. Mitnitski, A. J. Mogilner, and K. Rockwood, *The Scientific World* **1**, 323 (2001).
- [11] L. P. Fried, C. M. Tangen, J. Walston, A. B. Newman, C. Hirsch, J. Gottdiener, T. Seeman, R. Tracy, W. J. Kop, G. Burke, and M. A. McBurnie, *The Journals of Gerontology: Series A* **56**, M146 (2001).
- [12] E. Pierson, P. W. Koh, T. Hashimoto, D. Koller, and P. Liang, *Proc Mach Learn Res* **89**, 97 (2019).
- [13] K. Avchaciov, M. P. Antoch, E. L. Andrianova, A. E. Tarkhov, L. I. Menshikov, O. Burmistrova, A. V. Gudkov, and P. O. Fedichev, *bioRxiv* (2020), <http://dx.doi.org/10.1101/2020.01.23.917286>.
- [14] S. Farrell, G. Stubbings, K. Rockwood, A. Mitnitski, and A. Rutenberg, *Mechanisms of Ageing and Development* **193**, 111403 (2021).
- [15] Y.-Y. Liu, S. Li, F. Li, L. Song, and J. M. Rehg, *Advances in Neural Information Processing Systems*, 3600 (2015).
- [16] P. Schulam and S. Suchi, *Advances in Neural Information Processing Systems* **28** (2015).
- [17] A. M. Alaa and M. van der Schaar, (2018), [arXiv:1810.10489v1](https://arxiv.org/abs/1810.10489v1).
- [18] C. K. Fisher, A. M. Smith, and J. R. Walsh, *Scientific Reports* **9**, 1 (2019).
- [19] J. R. Walsh, A. M. Smith, Y. Pouliot, D. Li-Bland, A. Loukianov, and C. K. Fisher, (2020), [arXiv:2002.02779v1](https://arxiv.org/abs/2002.02779v1).
- [20] B. Lim and M. van der Schaar, *Proceeding of Machine Learning Research* **85**, 137 (2018).
- [21] A. I. Yashin, K. G. Arbeev, I. Akushevich, A. Kulminski, L. Akushevich, and S. V. Ukraintseva, *Mathematical Biosciences* **208**, 538 (2007).
- [22] K. G. Arbeev, I. Akushevich, A. M. Kulminski, S. V. Ukraintseva, and A. I. Yashin, *Frontiers in Public Health* **2** (2014).
- [23] I. Y. Zhbannikov, K. Arbeev, I. Akushevich, E. Stallard, and A. I. Yashin, *BMC Bioinformatics* **18** (2017).
- [24] S. Farrell, A. Mitnitski, K. Rockwood, and A. Rutenberg, *Scientific Reports*, 19833 (2020).
- [25] S. Clemens, A. Phelps, Z. Oldfield, M. Blake, A. Os-kala, M. Marmot, N. Rogers, J. Banks, A. Steptoe, and J. Nazroo, *UK Data Service. 30th Edition* **5050** (2019), <http://doi.org/10.5255/UKDA-SN-5050-17>.
- [26] C. Rudin, *Nature Machine Intelligence* **1**, 206 (2019).
- [27] C. Rackauckas, Y. Ma, J. Martensen, C. Warner, K. Zubov, R. Supekar, D. Skinner, A. Ramadhan, and A. Edelman, (2020), [arXiv:2001.04385](https://arxiv.org/abs/2001.04385) [cs.LG].
- [28] A. Karpatne, G. Atluri, J. H. Faghmous, M. Steinbach, A. Banerjee, A. Ganguly, S. Shekhar, N. Samatova, and V. Kumar, *IEEE Transactions on knowledge and data engineering* **29**, 2318 (2017).
- [29] A. B. Mitnitski, A. D. Rutenberg, S. Farrell, and K. Rockwood, *Biogerontology* **18**, 433 (2017).
- [30] A. D. Rutenberg, A. B. Mitnitski, S. G. Farrell, and K. Rockwood, *Experimental Gerontology* **107**, 126 (2018).
- [31] Y. L. Qiu, H. Zheng, and O. Gevaert, *GigaScience* **9** (2020).
- [32] Y. Gong, H. Hajimirsadeghi, J. He, M. Nawhal, T. Durand, and G. Mori, in *Proceedings of The 2nd Symposium on Advances in Approximate Bayesian Inference*, Proceedings of Machine Learning Research, Vol. 118, edited by C. Zhang, F. Ruiz, T. Bui, A. B. Dieng, and D. Liang (PMLR, 2020) pp. 1–17.
- [33] D. Rezende and S. Mohamed, in *Proceedings of the 32nd International Conference on Machine Learning*, Proceedings of Machine Learning Research, Vol. 37, edited by F. Bach and D. Blei (PMLR, Lille, France, 2015) pp. 1530–1538.
- [34] A. I. Yashin and K. G. Manton, *Statistical Science* **12**, 20 (1997).
- [35] A. I. Yashin, K. G. Arbeev, I. Akushevich, A. Kulminski, S. V. Ukraintseva, E. Stallard, and K. C. Land, *Physics of Life Reviews* **9**, 177 (2012).
- [36] D. M. Blei, A. Kucukelbir, and J. D. McAuliffe, *Journal of the American Statistical Association* **112**, 859 (2017).
- [37] L. Antolini, P. Boracchi, and E. Biganzoli, *Statistics in Medicine* **24**, 3927 (2005).
- [38] S. van Buuren and K. Groothuis-Oudshoorn, *Journal of Statistical Software, Articles* **45**, 1 (2011).
- [39] D. J. Stekhoven and P. Bühlmann, *Bioinformatics* **28**, 112 (2011).
- [40] E. Graf, C. Schmoor, W. Sauerbrei, and M. Schumacher, *Statistics in Medicine* **18**, 2529 (1999).
- [41] H. Haider, B. Hoehn, S. Davis, and R. Greiner, *Journal of Machine Learning Research* **21**, 1 (2020).

- [42] D. Lopez-Paz and M. Oquab, in *5th International Conference on Learning Representations, ICLR 2017, Toulon, France, April 24-26, 2017, Conference Track Proceedings* (OpenReview.net, 2017).
- [43] D. Bertolini, A. D. Loukianov, A. M. Smith, D. Li-Bland, Y. Pouliot, J. R. Walsh, and C. K. Fisher, (2020), arXiv:2012.13455 [cs.LG].
- [44] Y.-Z. Chen and Y.-C. Lai, *Physical Review E* **97**, 032317 (2018).
- [45] Y. Rubanova, T. Q. Chen, and D. Duvenaud, *NeurIPS* (2019).
- [46] E. De Brouwer, J. Simm, A. Arany, and Y. Moreau, *NeurIPS*, 7377 (2019).
- [47] J. Jordon, A. Wilson, and M. van der Schaar, (2020), arXiv:2012.04580 [cs.LG].
- [48] A synthetic population of nearly 10^7 individuals with 20 years of annually sampled trajectories from baseline is available at <https://zenodo.org/record/4733386>.
- [49] B. Zhang and S. Horvath, *Statistical Applications in Genetics and Molecular Biology* **4**, 1 (2005).
- [50] C. García-Peña, R. Ramírez-Aldana, L. Parra-Rodríguez, J. C. Gómez-Verján, M. U. Pérez-Zepeda, and L. M. Gutiérrez-Robledo, *Experimental Gerontology* **128**, 110747 (2019).
- [51] C. W. J. Granger, *Information and Control* **6**, 28 (1963).
- [52] K. J. Friston, L. Harrison, and W. Penny, *NeuroImage* **19**, 1273 (2003).
- [53] K. J. Friston, K. H. Preller, C. Mathys, H. Cagnan, J. Heinze, A. Razi, and P. Zeidman, *NeuroImage* **199**, 730 (2019).
- [54] L. E. Davies, G. Spiers, A. Kingston, A. Todd, J. Adamson, and B. Hanratty, *Journal of the American Medical Directors Association* **21**, 181 (2020).
- [55] A. J. Miller, O. Theou, M. McMillan, S. E. Howlett, K. K. Tennankore, and K. Rockwood, *Journals of Gerontology A* **72**, 376 (2017).
- [56] D. R. Cox, *Journal of the Royal Statistical Society. Series B* **34**, 187 (1972).
- [57] B. Lehallier, D. Gate, N. Schaum, T. Nanasi, S. E. Lee, H. Yousef, P. M. Losada, D. Berdnik, A. Keller, J. Verghese, S. Sathyan, C. Franceschi, S. Milman, N. Barzilai, and T. Wyss-Coray, *Nature Medicine* **25**, 1843 (2019).
- [58] S. Ahadi, W. Zhou, S. M. S.-F. Rose, M. R. Sailani, K. Contrepois, M. Avina, M. Ashland, A. Brunet, and M. Snyder, *Nature Medicine* **26**, 83 (2020).
- [59] K. Cho, B. van Merriënboer, C. Gulcehre, D. Bahdanau, F. Bougares, H. Schwenk, and Y. Bengio, in *Proceedings of the 2014 Conference on Empirical Methods in Natural Language Processing (EMNLP)* (Association for Computational Linguistics, Doha, Qatar, 2014) pp. 1724–1734.
- [60] A. Golightly and D. Wilkinson, *Computational Statistics & Data Analysis* **52**, 1674–1693 (2008).
- [61] G. A. Whitaker, A. Golightly, R. J. Boys, and C. Sherlock, *Bayesian Analysis* **12**, 435 (2017).
- [62] C. Archambeau, M. Opper, Y. Shen, D. Cornford, and J. S. Shawe-Taylor, *Advances in Neural Information Processing Systems* **20**, 17 (2008).
- [63] M. Opper, *Annalen der Physik* **531**, 1800233 (2019).
- [64] X. Li, T.-K. L. Wong, R. T. Q. Chen, and D. Duvenaud, arXiv **2001.01328** (2020).
- [65] L. Dinh, J. Sohl-Dickstein, and S. Bengio, in *5th International Conference on Learning Representations, ICLR 2017, Toulon, France, April 24-26, 2017, Conference Track Proceedings* (OpenReview.net, 2017).
- [66] D. P. Kingma and J. Ba, *Proceedings of the 3rd International Conference on Learning Representations* (2015).
- [67] A. Rößler, *SIAM J. Numer. Anal.* **48**, 922 (2010).
- [68] T. Hastie, R. Tibshirani, and J. Friedman, *The Elements of Statistical Learning*, Springer Series in Statistics (Springer New York Inc, New York, NY, USA, 2001).
- [69] F. Pedregosa, G. Varoquaux, A. Gramfort, V. Michel, B. Thirion, O. Grisel, M. Blondel, P. Prettenhofer, R. Weiss, V. Dubourg, J. Vanderplas, A. Passos, D. Cournapeau, M. Brucher, M. Perrot, and E. Duchesnay, *Journal of Machine Learning Research* **12**, 2825 (2011).
- [70] N. E. Breslow, *Journal of the Royal Statistical Society: B* **34**, 216 (1972).
- [71] H. Zou and T. Hastie, *Journal of the Royal Statistical Society: B* **67**, 301 (2005).

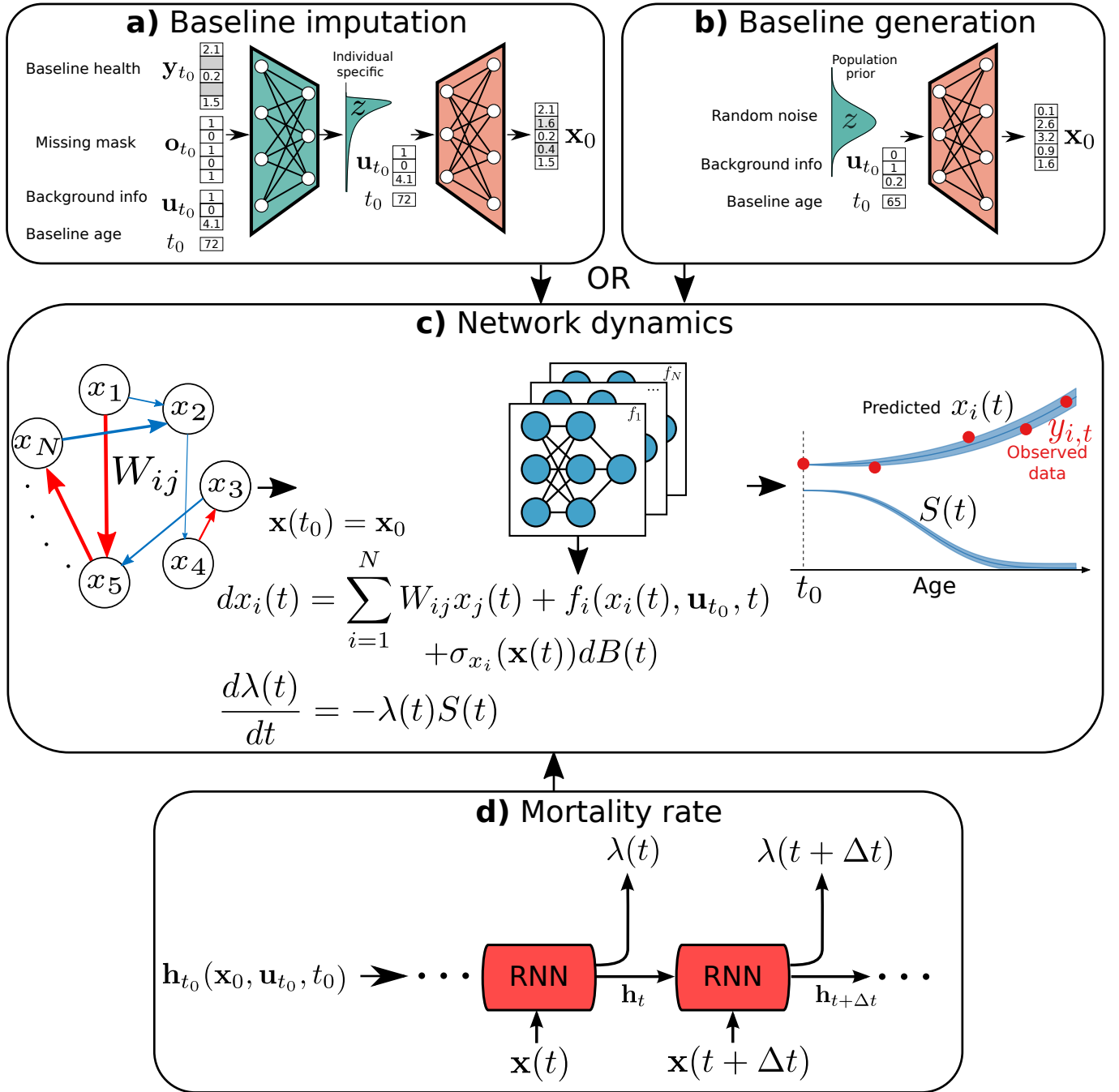


FIG. 1. **DJIN model of aging.** **a)** Baseline imputation is performed using the baseline health measurement \mathbf{y}_{t_0} , missing mask \mathbf{o}_{t_0} , background health information \mathbf{u}_{t_0} , and baseline age t_0 as input to an encoder neural network (green) that parameterizes a latent distribution. Sampling from this latent distribution and using a decoder neural network (orange) gives an imputed complete baseline health-state \mathbf{x}_0 . **b)** Baseline generation conditional on background health information \mathbf{u}_{t_0} , and baseline age t_0 can be used instead of imputation. The population latent distribution is sampled and used with the same decoder neural network (orange) to produce a synthetic baseline health state \mathbf{x}_0 . **c)** Network dynamics stochastically evolve the health state $\mathbf{x}(t)$ in time starting from the baseline state \mathbf{x}_0 . The stochastic dynamics are modeled with a stochastic differential equation which includes the pairwise network interactions with connection weight matrix \mathbf{W} , general diagonal terms $f_i(x_i(t), \mathbf{u}_{t_0}, t)$ parameterized as neural networks, and a diagonal covariance matrix for the noise $\sigma_x(\mathbf{x})$ also parameterized with a neural network. **d)** The survival function evolves in time based on the state and history of the health state \mathbf{x} using a recurrent neural network (RNN). The initial state of the RNN, \mathbf{h}_{t_0} , is set using the background health information \mathbf{u}_{t_0} , baseline age t_0 , and \mathbf{x}_0 . Details are provided in the Methods. The code for our model is available at <https://github.com/Spencerfar/djin-aging>.

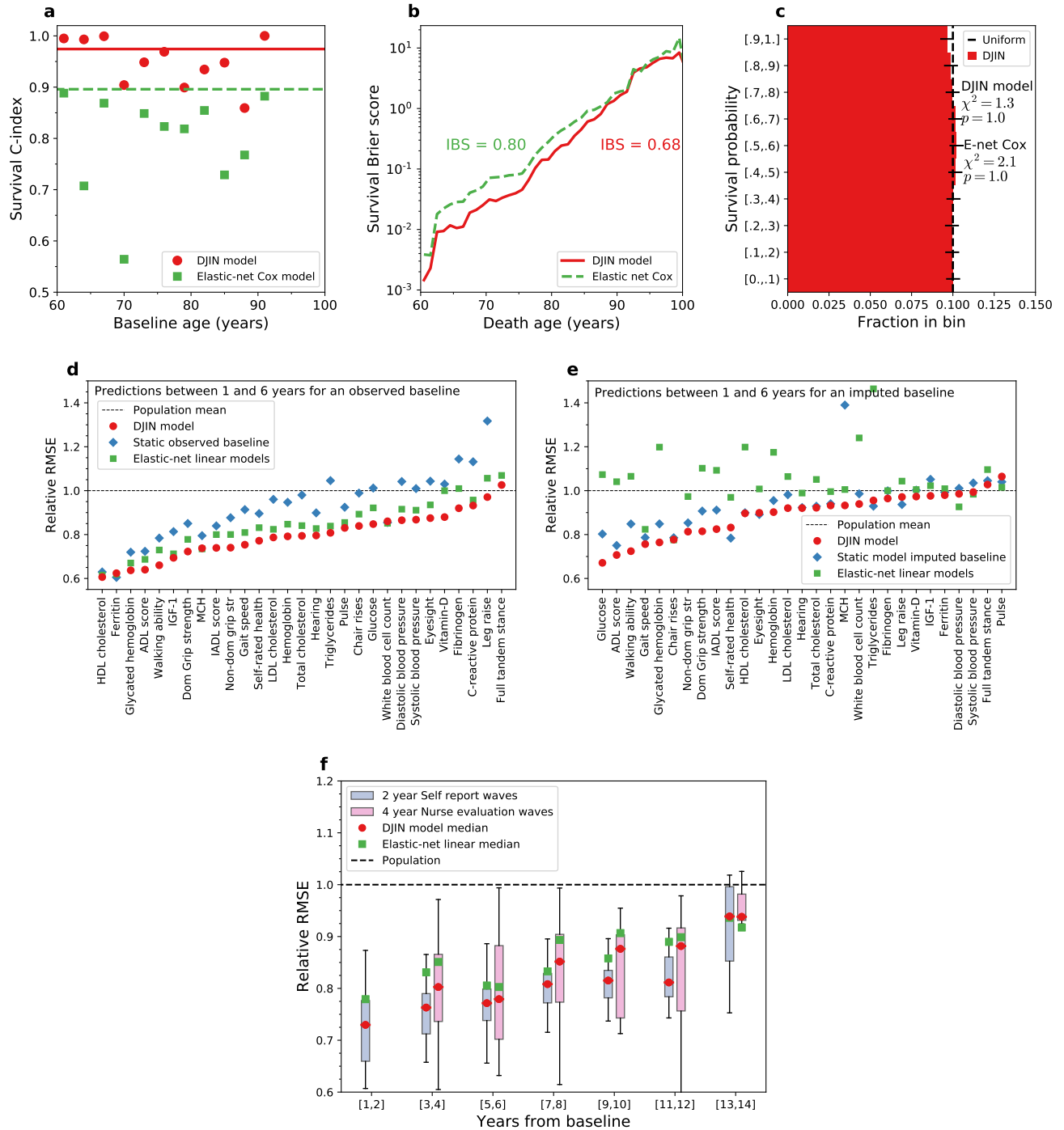


FIG. 2. Model predictions and validation. **a**) Time-dependent C-index stratified vs age (points) and for all ages (line). Results are shown for our model (red) and a Elastic net Cox model (green). (Higher scores are better). **b**) Brier scores for the survival function vs death age. Integrated Brier scores (IBS) over the full range of death ages are also indicated. (Lower scores are better). **c**) D-calibration of survival predictions. Error bars show the standard deviation. Estimated survival probabilities are expected to be uniformly distributed (dashed black line). We use Pearson's χ^2 test to assess the distribution of survival probabilities for our network model ($\chi^2 = 1.3$, $p = 1.0$) and an elastic net Cox model ($\chi^2 = 2.1$, $p = 1.0$). (Higher p-values and smaller χ^2 statistics are better). **d**) RMSE scores when the baseline value is observed for each health variable for predictions between 1 and 6 years from baseline, scaled by the RMSE score from the age and sex dependent population mean (relative RMSE scores). We show the predictions from our model starting the baseline value (red circles), predictions assuming a static baseline value (blue squares), and 29 distinct elastic-net linear models trained separately for each of the variables (green squares). The DJIN predictions here come from the same model as for mortality and the elastic net Cox model is also a distinct model. (Lower RMSE is better). **e**) Relative RMSE scores when the when the baseline value for each health variable is imputed for predictions between 1 and 6 years from baseline. We show the predictions from our model starting from the imputed baseline value (red circles), predictions assuming a static imputed value (blue squares), and predictions assuming an elastic-net linear model (green squares). (Lower RMSE is better). **f**) RMSE score distributions over all health variables for increasing years of prediction from baseline. The median RMSE score is shown as a black dotted line between the boxes showing upper and lower quartiles. Whiskers show 1.5x the interquartile range from the box. (Lower RMSE is better). Self-report and nurse-evaluated waves have distinct patterns of missing variables; nurse-evaluated waves have higher missingness overall.

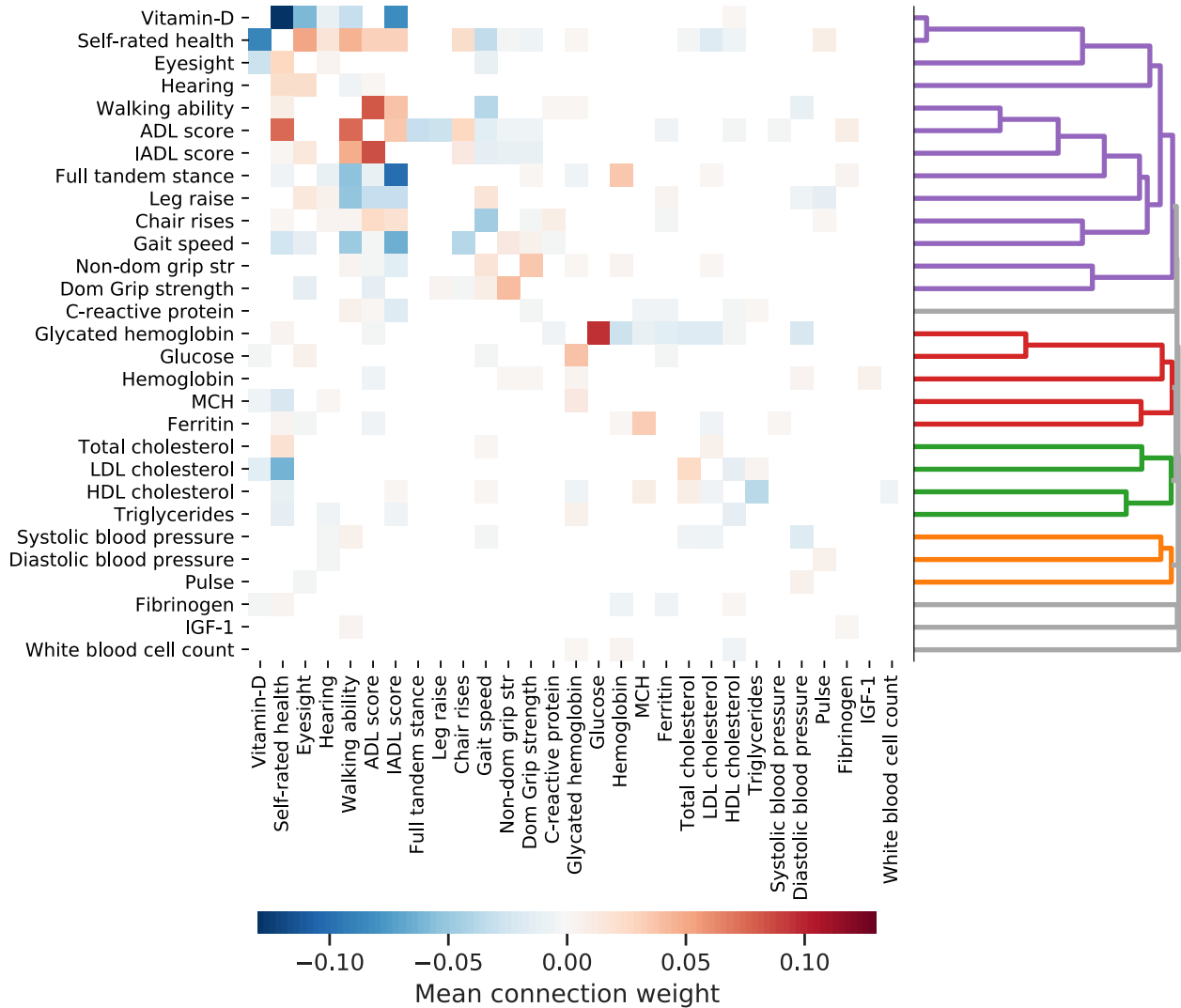


FIG. 3. **Inferred interaction network.** Heatmap of the posterior mean value of the robust network weights. Weight directions are read from the horizontal axis (j) towards the vertical (i), $W_{i \leftarrow j}$. The sign and color of the weight signify the direction of effect – a positive weight implies that an increase in a variable along the horizontal axis influences the vertical axis variable to increase. A negative weight implies that an increase in a variable along the horizontal axis influences the vertical axis variable to decrease. Hierarchical clustering is applied to the absolute posterior mean of the robust weights to create a dendrogram.

IV. METHODS

A. ELSA dataset

We use all 8 waves of the English Longitudinal study of Aging (ELSA) dataset [25] to train our model, with 25290 individuals. In Supplemental Table 1 we list all variables used. In Supplemental Fig. 1, we show the number of individuals for which the variable is available at different times from baseline. We extract 29 longitudinally observed continuous or discrete ordinal health variables (treated as continuous) and 19 background health variables (taken as constant with age). All individuals with missing sex or ethnicity are dropped. We set the gait speed of individuals with values above 4 meters per second to missing, due to a likely data error. Individuals with all ages missing are dropped, sporadic missing ages are imputed by assuming the age difference between waves is 2 years – the time difference in the design of the study. Ages and death ages for individuals above age 90 are also imputed this way in addition to the year that the wave occurred. Height is imputed with the last observation carried forward (the first value is imputed backwards if it is missing).

The data is randomly split into separate train (16689 individuals), validation (4173 individuals), and test sets (5216 individuals). The training set is used to train the model, the validation set is used for control of the optimization procedure during training (through a learning rate schedule, see Section IV F below), and the test set is used to evaluate the model after training. Individuals with fewer than 6 variables measured at age t_0 are dropped from the training and validation data. Individuals with fewer than 10 variables measured at age t_0 are dropped from the test data for predictions, while all individuals in the test data are used for population comparisons.

All variables are standardized to mean 0 and standard deviation 1 (computed from the training set); however variables with a skewed age-aggregated distribution $p(\mathbf{y})$ covering multiple orders of magnitude are first log-transformed. Log-scaled variables are indicated in Supplemental Table 1.

B. Data augmentation

Since some health variables are measured only at specific visits, using the first wave observed for the starting point of every individual forces some variables to be rarely observed at baseline, hindering imputation of variables that are only observed at later waves. To mitigate this and to augment the dataset, we replicate individuals to use all possible starting points, $t_k^{(m)}, k \in \{0, \dots, \text{argmax}_k(t_k^{(m)})\}$. Since individuals have different numbers of observed times we weight individuals in the likelihood who have multiple times available by $s^{(m)} = 1/(\text{argmax}_k(t_k^{(m)}) + 1)$. This helps to prevent the over-weighting of individuals with many possible starting times. Nevertheless, we still assume that replicated individuals are independent in the likelihood.

To further augment the available data, we artificially corrupt the input data for training by masking each observed health variable at baseline with probability 0.9. This allows more distinct “individuals” for imputation of the baseline state, and allows us to use add self-supervision for these artificially missing values by training to reconstruct the artificially corrupted states.

C. DJIN model

We model the temporal dynamics of an individual’s health state with continuous-time stochastic dynamics described with stochastic differential equations (SDEs). These SDEs include linear pair-wise interactions between the variables to form a network with a weight matrix \mathbf{W} . We assume the observed health variables \mathbf{y}_t are noisy observations of the underlying latent state variables $\mathbf{x}(t)$, which evolves according to these network SDEs. This allows us to separate measurement noise from the noise intrinsic to the stochastic dynamics of these variables.

These SDEs for $\mathbf{x}(t)$ start from the baseline state \mathbf{x}_0 , which is imputed from the available observed health state \mathbf{y}_t . This imputation process is done using a normalizing-flow variational auto-encoder (VAE) [33]. In this approach, we encode the available baseline information into a latent distribution for each individual, and decode samples from this distribution to perform multiple imputation. The normalizing-flow VAE allows us to flexibly model this latent distribution. The details are described in Section IV D below.

Our model is described by the following equations:

$$\begin{aligned}
(1) \quad & \boldsymbol{\theta} = \{\mathbf{W}, \sigma_{\mathbf{y}}, \sigma_{\mathbf{x}}, \boldsymbol{\theta}_{\lambda}, \boldsymbol{\theta}_p, \boldsymbol{\theta}_f\}. && \text{(Parameters)} \\
(2) \quad & \mathbf{z}, \boldsymbol{\theta} \sim p(\mathbf{z})p(\boldsymbol{\theta}), && \text{(Prior)} \\
(3) \quad & \mathbf{x}_0 = \mathbf{o}_{t_0} \odot \mathbf{y}_{t_0} + (1 - \mathbf{o}_{t_0}) \odot \tilde{\mathbf{x}}_0, \quad \tilde{\mathbf{x}}_0 \sim \mathcal{N}(\mathbf{x}_0 | \boldsymbol{\mu}_{\mathbf{x}}(\mathbf{z}, \mathbf{u}_{t_0}, t_0, \boldsymbol{\theta}_p), \boldsymbol{\sigma}_{\mathbf{y}}^2), && \text{(Imputation)} \\
(4) \quad & dx_i(t) = \sum_{j=1}^N W_{ij} x_j(t) + f_i(x_i(t), \mathbf{u}_{t_0}, t; \boldsymbol{\theta}_{f_i}) + \sigma_{x_i}(\mathbf{x}(t)) dB(t), \quad \mathbf{x}(t_0) = \mathbf{x}_0, && \text{(Dynamics)} \\
(5) \quad & \mathbf{y}_t \sim \mathcal{N}(\boldsymbol{\psi}^{-1}(\mathbf{x}(t)), \text{diag}(\sigma_{\mathbf{y}}^2)), && \text{(Health observation)} \\
(6) \quad & S(t) = \exp\left(-\int_{t_0}^t \lambda(\{\mathbf{x}(\tau)\}_{\tau \leq t'}, \mathbf{u}_{t_0}, t'; \boldsymbol{\theta}_{\lambda}) dt'\right), && \text{(Survival)} \\
(7) \quad & a \sim \lambda(\{\mathbf{x}(\tau)\}_{\tau \leq a}, \mathbf{u}_{t_0}, a; \boldsymbol{\theta}_{\lambda}) S(a), && \text{(Survival observation)} \\
(8) \quad & p(\mathbf{z}, \{\mathbf{x}(t)\}_t, \boldsymbol{\theta} | \{\mathbf{y}_{t_k}\}_k, \mathbf{u}_{t_0}, \{\mathbf{o}_{t_k}\}_k, t_0, a, c) \propto p(\boldsymbol{\theta}) p(\mathbf{z}) p(\mathbf{x}_0 | \mathbf{z}, \mathbf{u}_{t_0}) \times && \text{(Inference)} \\
& p(\{\mathbf{x}(t)\}_t | \mathbf{x}_0, \mathbf{u}_{t_0}, t_0, \boldsymbol{\theta}) p(a, c | \{\mathbf{x}(t)\}_t, \mathbf{u}_{t_0}, t_0, \boldsymbol{\theta}) \prod_k p(\mathbf{y}_{t_k} | \{\mathbf{x}(t_k)\}_k, \mathbf{o}_{t_k}, \boldsymbol{\theta}),
\end{aligned}$$

Model parameters ($\boldsymbol{\theta}$) include the explicit network of interactions between health variables (W), measurement noise (σ_y) and dynamical SDE noise (σ_x), and network weights for mortality RNN ($\boldsymbol{\theta}_{\lambda}$), imputation VAE ($\boldsymbol{\theta}_p$), and dynamical SDE ($\boldsymbol{\theta}_f$). Equation (2) represents priors on the model parameters and latent state \mathbf{z} . We use Laplace($\mathbf{w}|0, 0.05$) priors for the network weights and Gamma($\sigma_{\mathbf{y}}|1, 25000$) priors for the measurement noise scale parameters. We use a normal (Gaussian) prior distribution for the latent space \mathbf{z} . We assume uniform priors for all other parameters.

In Equation (3) we sample the baseline state. The distribution for \mathbf{x}_0 given \mathbf{z} is modeled as Gaussian with mean computed from the decoder neural network and the same standard deviation as the measurement noise, $\mathcal{N}(\boldsymbol{\mu}_{\mathbf{x}}(\mathbf{z}, \mathbf{u}_{t_0}, t_0), \boldsymbol{\sigma}_{\mathbf{y}}^2)$. The missing value imputation and the dynamics model are trained together simultaneously (see details below). This allows us to utilize the additional longitudinal information for training the imputation method, and helps to avoid an imputed baseline state that leads to poor trajectory or survival predictions.

Equation (4) describes the SDE network dynamics, starting from the imputed baseline state. We capture single-variable trends with the non-linear $f_i(x_i(t), \mathbf{u}_{t_0}, t)$, and couple the components of $\mathbf{x}(t)$ linearly by the directed interaction matrix \mathbf{W} , which represents the strength of interactions between the health variables. In this way, f_i can be thought of as a non-linear function for the diagonal components of this matrix, while \mathbf{W} gives linear pair-wise interactions for the off-diagonal components. The intrinsic diffusive noise in the health trajectories is modeled with Brownian motion with Gaussian increments $dB(t)$ and strength $\sigma_{\mathbf{x}}$. The functions f_i and $\sigma_{\mathbf{x}}$ are parameterized with neural networks.

Equation (5) describes the Gaussian observation model for the observed health state. Measurement noise here is separate from diffusive noise $dB(t)$ in the SDE from Equation (4). The component-wise transformation $\boldsymbol{\psi}$ applies a log-scaling to skewed variables (indicated in Table 1 in Supplemental material) and z-scores all variables.

Equation (6) describes the survival probability as computed with a recurrent neural network (RNN) for the mortality hazard rate λ . The RNN allows us to use the stochastic trajectory for the computation of the hazard rate (i.e. it has some memory of health at previous ages), rather than imposing a memory-free process where the hazard rate only depends on the health state at the current age. We use a 2-layer Gated Recurrent Unit (GRU [59]) for the RNN, with hidden state \mathbf{h}_t . The initial hidden state \mathbf{h}_0 is inferred from the initial health variables $\mathbf{x}(t_0)$, background health information \mathbf{u}_{t_0} , and baseline age t_0 , with a neural network $\mathbf{h}_0 = H(\mathbf{x}(t_0), \mathbf{u}_{t_0}, t_0)$. Equation (7) describes the observation model for survival with age of death or last age known alive $a = \max(t_d, t_c)$, and censoring indicator c .

Instead of a maximum likelihood point estimate of the network and other parameters of the model, we use a Bayesian approach. This allows us to infer the posterior distribution of the health trajectories and interaction network, and so lets us estimate the robustness of the inferred network and the distribution of possible predicted trajectories, given the observed data. In Equation (8) we show the form of the unnormalized posterior distribution.

D. Variational approximation for scalable Bayesian inference

While sampling based methods of inference for SDE models do exist [60, 61], these are generally not scalable to large datasets or to models with many parameters. Instead, we use an approximate variational inference approach [62, 63]. We assume a parametric form of the posterior that is optimized to be close to the true posterior. While

variational approximations tend to underestimate the width of posterior distributions and simplify correlations, they typically capture the mean [36].

Our factorized mean-field variational approximation to the posterior in Equation (8) is

$$\begin{aligned} q(\mathbf{z}, \mathbf{x}(t), \boldsymbol{\theta} | \mathbf{y}_0, \mathbf{u}_{t_0}, \mathbf{o}_{t_0}, t_0, \phi) &= q(\mathbf{z} | \mathbf{y}_0, \mathbf{u}_{t_0}, \mathbf{o}_{t_0}, t_0, \phi_z) q(\mathbf{x}(t) | \mathbf{x}_0, \mathbf{u}_{t_0}, t, \phi_x) q(\boldsymbol{\theta} | \phi_\theta), \\ \{\mathbf{x}(t)\}_t \sim q(\mathbf{x}(t) | \mathbf{x}_0, \mathbf{u}_{t_0}, t, \phi_x) &\implies d\mathbf{x}(t) = \bar{\mathbf{W}}\mathbf{x} + \mathbf{f}(\mathbf{x}, \mathbf{u}_{t_0}, t) + \mathbf{g}(\mathbf{x}, \mathbf{u}_{t_0}, t; \phi) + \boldsymbol{\sigma}_x d\mathbf{B}(t). \end{aligned} \quad (9)$$

Instead of assuming an explicit parametric form for $q(\mathbf{x}(t) | \phi_x)$, we instead assume the trajectories $\{\mathbf{x}(t)\}_t$ are described by samples from a posterior SDE with drift modified by including a small fully connected neural network \mathbf{g} [64]. $\bar{\mathbf{W}}$ is the posterior mean of the network weights. The functional form of the posterior drift is both more general and more easily trainable than the network SDE in Equation 4, but ultimately is forced to be close to the network dynamics in Equation (4) by the loss function. The loss function for this approach has been previously derived [62, 63]. The imputed baseline states \mathbf{x}_0 are averaged over.

For the latent state \mathbf{z} , the approximate posterior takes the form

$$\boldsymbol{\mu}_z, \boldsymbol{\sigma}_z, \boldsymbol{\gamma}_z = \text{Encoder}(\tilde{\mathbf{y}}_{t_0}, \mathbf{o}_{t_0}, \mathbf{u}_{t_0}, t_0, \phi_z), \quad (10)$$

$$\tilde{\mathbf{y}}_{t_0} = \mathbf{o}_{t_0} \odot \mathbf{y}_{t_0} + (1 - \mathbf{o}_{t_0}) \odot \epsilon_{\mathbf{y}_{s,t_0}, \text{pop}}, \quad (11)$$

$$q(\mathbf{z} | \mathbf{y}_{t_0}, \mathbf{u}_{t_0}, \mathbf{o}_{t_0}, t_0, \phi_z) \equiv q(\mathbf{z}^{(L)} | \tilde{\mathbf{y}}_{t_0}, \mathbf{u}_{t_0}, \mathbf{o}_{t_0}, t_0, \phi_z) = \mathcal{N}(\mathbf{z}^{(0)} | \boldsymbol{\mu}_z, \boldsymbol{\sigma}_z^2) \prod_{l=1}^L \left| \det \frac{\partial a^{(l)}(\mathbf{z}^{(l)}, \boldsymbol{\gamma}_z, \phi_z)}{\partial \mathbf{z}^{(l)}} \right|^{-1}, \quad (12)$$

where the functions $a^{(l)}$ are RealNVP normalizing flows [65] used to transform the Gaussian base distribution for $\mathbf{z}^{(0)}$ to the non-Gaussian posterior approximation, conditioned on the specific individual with $\boldsymbol{\gamma}_z$. These are invertible neural networks that transform probability distributions while maintaining normalization. In Equation 11 we fill in missing values in the observed health state since \mathbf{o} is a mask of observed variables and $\epsilon_{\mathbf{y}_{s,t_0}, \text{pop}}$ is sampled from a Gaussian distribution with the sex and age-dependent population mean and standard deviation. \odot is element-wise multiplication. These filled in values are temporarily input to the encoder neural network, and replaced after imputation.

The variational parameters of the approximate posterior ϕ are optimized to minimize the KL divergence between the approximation and the true posterior. This minimized KL divergence provides a lower bound to the model evidence that can be maximized,

$$\begin{aligned} \log p(\{\mathbf{y}_{t_k}\}_k | \mathbf{u}_{t_0}, \mathbf{o}_{t_0}, t_0) \geq \\ \mathbb{E}_{\boldsymbol{\theta}, \mathbf{z}, \mathbf{x}_0 | \mathbf{z}, \{\mathbf{x}(t)\}_t | \mathbf{x}_0} \left[\log \frac{p(\boldsymbol{\theta}) p(\mathbf{z}) p(\{\mathbf{x}(t)\}_t | \mathbf{x}_0, \mathbf{u}_{t_0}, \boldsymbol{\theta}) p(a, \delta | \{\mathbf{x}(t)\}_t, \mathbf{u}_{t_0}, t_0) \prod_k p(\mathbf{y}_{t_k} | \mathbf{x}(t_k), \mathbf{o}_{t_k}, \boldsymbol{\theta})}{q(\mathbf{z} | \mathbf{y}_0, \mathbf{u}_{t_0}, \mathbf{o}_{t_0}, t_0) q(\boldsymbol{\theta}) q(\{\mathbf{x}(t)\}_t | \mathbf{x}_0, \mathbf{u}_{t_0})} \right], \end{aligned} \quad (13)$$

where in the expectation $\boldsymbol{\theta}$, \mathbf{z} , and $\{\mathbf{x}(t)\}_t$ are sampled from their respective posterior distributions. The imputed baseline state is sampled as,

$$\boldsymbol{\mu}_x = \text{Decoder}(\mathbf{z}, \mathbf{u}_{t_0}, t_0) \quad (14)$$

$$\tilde{\mathbf{x}}_0 \sim \mathcal{N}(\boldsymbol{\mu}_x, \boldsymbol{\sigma}_y^2) \quad (15)$$

$$\mathbf{x}_0 = \mathbf{o}_{t_0} \odot \mathbf{y}_{t_0} + (1 - \mathbf{o}_{t_0}) \odot \tilde{\mathbf{x}}_0. \quad (16)$$

The final objective function to be maximized is \mathcal{L} , where the derivation is provided in the Supplemental Information. We obtain

$$\begin{aligned} \mathcal{L}(\phi) = \mathbb{E} \left[\sum_k \mathbf{o}_{t_k} \odot \log \mathcal{N}(\mathbf{y}_{t_k} | \mathbf{x}(t_k), \boldsymbol{\sigma}_y) \right. \\ \left. + \int_{t_0}^a \left\{ c \log S(a | \mathbf{x}(t), \mathbf{u}_{t_0}, t_0) + (1 - c) \left[\log \lambda(a | \mathbf{x}(t), \mathbf{u}_{t_0}, t_0) + \log S(a | \mathbf{x}(t), \mathbf{u}_{t_0}, t_0) \right] \right\} dt \right. \\ \left. - \frac{1}{2} \int_{t_0}^a \left\| \boldsymbol{\sigma}_x^{-1} \odot (\mathbf{W}\mathbf{x} - \bar{\mathbf{W}}\mathbf{x} - \mathbf{g}(\mathbf{x}, \mathbf{u}_{t_0}, t)) \right\|_2^2 dt \right] \\ - KL(q(\boldsymbol{\theta}) || p(\boldsymbol{\theta})) - KL(q(\mathbf{z}^{(0)} | \mathbf{y}_0, \mathbf{u}_{t_0}, \mathbf{o}_{t_0}, t_0) || p(\mathbf{z}^{(0)})) + \sum_{l=1}^L \log \left| \det \frac{\partial a^{(l)}(\mathbf{z}^{(l)}, \boldsymbol{\gamma}_z, \phi_z)}{\partial \mathbf{z}^{(l)}} \right|, \end{aligned} \quad (17)$$

as the loss function for each individual. This is for all individuals in the data multiplied by the sample weights $s^{(m)}$ for each individual m . To simplify the evaluation of \mathcal{L} and decrease the number of parameters, we assume independent

Gamma posteriors for each measurement error parameter σ_y with separate shape α_i and rate β_i . We also assume independent Laplace posteriors for each of the network weights W_{ij} with separate means \bar{W}_{ij} and scales b_{ij} . For the approximate distribution of all other parameters we use delta functions, and together with uniform priors this leads to simplifying the approach to just optimizing these parameters instead of optimizing variational parameters of the posterior.

E. Summarized training procedure

1. Pre-process data. Assign N dynamical health variables and B static health variables. Reserve validation and test data from training data.
2. Sample batch and apply masking corruption and temporarily fill in missing values with samples from the population distribution,

$$\begin{aligned}\tilde{\mathbf{y}}_{t_0} &= \mathbf{c} \odot \mathbf{o}_{t_0} \odot \mathbf{y}_{t_0} + (1 - \mathbf{c} \odot \mathbf{o}_{t_0}) \odot \epsilon_{\mathbf{y}_{s,t_0}, \text{pop}}, \\ \mathbf{c} &\sim \text{Bernoulli}(0.9).\end{aligned}\tag{18}$$

3. Impute initial state \mathbf{x}_0 with the VAE and compute the initial memory state of the mortality rate GRU,

$$\begin{aligned}\mathbf{z} &\sim q(\mathbf{z}|\tilde{\mathbf{y}}_{t_0}, \mathbf{u}_{t_0}, \mathbf{c} \odot \mathbf{o}_{t_0}, t_0), \\ \tilde{\mathbf{x}}_0 &\sim \mathcal{N}(\mathbf{x}_0|\boldsymbol{\mu}_{\mathbf{x}}(\mathbf{z}, \mathbf{u}_{t_0}, t_0), \boldsymbol{\sigma}_{\mathbf{y}}^2) \\ \mathbf{x}_0 &= \mathbf{o}_{t_0} \odot \mathbf{y}_{t_0} + (1 - \mathbf{o}_{t_0}) \odot \tilde{\mathbf{x}}_0, \\ \mathbf{h}_{t_0} &= \mathbf{H}(\mathbf{x}_0, \mathbf{u}_{t_0}, t_0).\end{aligned}\tag{19}$$

4. Sample trajectory from the SDE solver for the posterior SDE and compute mortality rate from GRU,

$$\begin{aligned}\{\mathbf{x}(t)\}_t &= \text{SDESolver}(\mathbf{x}_0, \mathbf{u}_{t_0}, t_0), \\ \{S(t)\}_t &= \text{GRU}(\{\mathbf{x}(t)\}_t|\mathbf{h}_{t_0}).\end{aligned}\tag{20}$$

5. Compute the gradient of the objective function (Equation 17) and update parameters, returning to step 2 until training is complete.
6. Evaluate model performance on test data.

F. Network architecture and Hyperparameters

The different neural networks used are summarized in Supplemental Table 2. We use ELU activation functions for most hidden layer non-linearities, unless specified otherwise. We have $N = 29$ dynamical health variables, and $B = 19$ static health variables. Additionally, we append a mask to the static health variables indicating which are missing, of size 17.

The functions f_i in Equation (4) are feed-forward neural networks with input size $2 + B + 17$, hidden layer size 12, and output size 1. Each $f_i, i \in \{1, \dots, N\}$ has its own weights. The noise function $\boldsymbol{\sigma}_{\mathbf{x}}$ has input size N , hidden layer size N , and output size N . The posterior drift \mathbf{g} is a fully-connected feed-forward neural network with input size $N + B + 1 + 17$, hidden layer size 8, and output size N . The VAE encoder has input size $2N + B + 1 + 17$, hidden layer sizes 95 and 70, and output size 40, with batch normalization applied before the activation functions for each hidden layer. The VAE decoder has input size $20 + B + 17$, hidden layer size 65, and output size N with batch normalization applied before the activation for the hidden layer. The size of the latent state \mathbf{z} is 20. The mortality rate λ is a 2-layer GRU [59] with a hidden layer sizes of 25 and 10.

We use 3 normalizing flow networks to transform the latent distribution from the Gaussian $\mathbf{z}^{(0)}$ to \mathbf{z} . We use RealNVP normalizing flow networks [65] with layer sizes 30, 24, and 10 with batch normalization before a Tanh activation function for the hidden layer. The size of $\boldsymbol{\gamma}_{\mathbf{z}}$ is 10.

We use batchsize of 1000 and learning rate 10^{-2} with the ADAM optimizer [66]. We decay the learning rate by a factor of 0.5 at loss plateaus lasting for 40 or more epochs. We use KL-annealing with β increasing linearly from 0 to 1 during the first 300 epochs for the KL loss terms for $q(\mathbf{x}(t))$ and $q(\mathbf{z}(t))$, and increase linearly from 0 to 1 from 300 to 500 epochs for the KL terms for the prior on \mathbf{W} . SDEs are solved with the strong order 1.0 stochastic Runge-Kutta method [67] with a constant time-step of 0.5 years. Integrals in the likelihood are computed with the trapezoid method using the same discretization as the dynamics.

G. Evaluation metrics

1. RMSE scores

Longitudinal health trajectory predictions are assessed with the Root-Mean-Square Error (RMSE) of the predictions with respect to the observed values. The RMSE is evaluated for each health variable and is weighted by the sample weights $s^{(m)}$. We compute these RMSE values for predictions for a specific age t_k ,

$$\text{RMSE}_i(t_k) = \sqrt{\frac{1}{M} \sum_{m=1}^M \sum_{k:t_k \geq t} s^{(m)} (\psi_i^{-1}(x_i(t_k)) - y_{i,t_k})^2}, \quad (21)$$

where the inverse transform ψ_i^{-1} reverse any log-scaling and the z-scoring performed on the variables.

2. Time-dependent C-index

Our model contains complex time-dependent effects where survival curves can potentially intersect, so we use a time-dependent C-index [37],

$$\begin{aligned} C_{\text{td}} &= \Pr(\hat{S}^{(m_1)}(a^{(m_1)}) < \hat{S}^{(m_2)}(a^{(m_1)}) | a^{(m_1)} < a^{(m_2)}, c^{(m_1)} = 0) \\ &= \frac{\sum_{m_1, m_2} s^{(m_1)} s^{(m_2)} \delta[\hat{S}^{(m_1)}(a^{(m_1)}) < \hat{S}^{(m_2)}(a^{(m_1)})] \delta[a^{(m_1)} < a^{(m_2)}] \delta[c^{(m_1)} = 0]}{\sum_{m_1, m_2} s^{(m_1)} s^{(m_2)} \delta[a^{(m_1)} < a^{(m_2)}] \delta[c^{(m_1)} = 0]}, \end{aligned} \quad (22)$$

where $s^{(m)}$ are individual sample weights. We denote death ages by t_d and censoring ages by t_c , and define $a^{(m)} = \min(t_c^{(m)}, t_d^{(m)})$ as the last observed age for censored individuals ($\delta^{(m)} = 0$) or the death age for uncensored individuals ($\delta^{(m)} = 1$).

3. Brier score

The Brier score compares predicted individual survival probabilities to the exact survival curves, i.e. a step function where $S = 1$ while the individual is alive, and $S = 0$ when the individual is dead. The censoring survival function $G(t)$ is computed from the Kaplan-Meier estimate of the censoring distribution (using censoring as events rather than the death [40]), which is used to weight the individuals to account for censoring. Then the Brier score is computed for all possible death ages,

$$\text{BS}(t) = \frac{1}{M} \sum_m s^{(m)} \left[\frac{\delta(a^{(m)} \leq t, c^{(m)} = 0) (S^{(m)}(t))^2}{G(a^{(m)})} + \frac{\delta(a^{(m)} > t) (1 - S^{(m)}(t))^2}{G(t)} \right]. \quad (23)$$

4. D-calibration

For well-calibrated survival probability predictions, we expect $p\%$ of individuals to have survived past the p th quantile of the survival distribution. This can be evaluated using D-calibration, and we follow the previously developed procedure [41] for computing the D-calibration statistic. The result is a discrete distribution that should match a uniform distribution if the calibration is perfect.

We use a χ^2 test to compare to the uniform distribution. Using 10 bins, we use a χ^2 test with 9 degrees of freedom. Larger p-values (and smaller χ scores) indicate that the survival probabilities are more uniformly distributed, as desired.

5. 2-sample classification tests

To assess the quality of our synthetic population, we train a logistic regression classifier and evaluate its ability to differentiate between the observed and synthetic populations [18, 19, 42, 43]. Ideally, a synthetic population would be indistinguishable from the observed population, giving a classification accuracy of 50%.

Our classifier takes the current age t , the synthetic or observed health variables \mathbf{y}_t , and the background health information variables \mathbf{u}_{t_0} , and then outputs the probability of being a synthetic individual or a real observed individual from the data-set. Missing values in the observed population are imputed with the sex and age dependent population mean, and these same values are applied to the synthetic health trajectories by masking the predicted values.

6. Hierarchical clustering

We perform hierarchical clustering on the network weights \mathbf{W} . This is done by constructing a dissimilarity matrix,

$$\begin{aligned}\boldsymbol{\omega} &= (\mathbf{W}^T + \mathbf{W})/2, \\ \mathbf{D} &= \max(\boldsymbol{\omega}) - \boldsymbol{\omega},\end{aligned}$$

and then using this dissimilarity matrix \mathbf{D} to perform agglomerative clustering with the average linkage [68]. We use the Scikit-learn [69] package.

H. Comparison with linear models

1. Imputation for comparison models

For the linear survival and longitudinal models, we use MICE for imputation [38] with a random forest model [39]. We impute with the mean of the estimated values. We use 40 trees and do a hyperparameter search over the maximum tree depth. We use the Scikit-learn [69] package.

2. Proportional hazards survival model

To compare with a suitable baseline model for survival predictions, we use a proportional hazards model [56] with the Breslow baseline hazard estimator [70]:

$$\begin{aligned}\lambda(t|t_0, \mathbf{y}_{t_0}, \mathbf{u}_{t_0}) &= \exp(\beta_0 t_0 + \boldsymbol{\beta}_y \cdot \mathbf{y}_{t_0} + \boldsymbol{\beta}_u \cdot \mathbf{u}_{t_0}), \\ S(t|t_0, \mathbf{y}_{t_0}, \mathbf{u}_{t_0}) &= \exp(-\hat{\Lambda}_0^{\text{Br}}(t)\lambda(t|t_0, \mathbf{y}_{t_0}, \mathbf{u}_{t_0})).\end{aligned}\tag{24}$$

We include elastic net regularization [71] for the coefficients of the covariates.

3. Linear trajectory model

We use a simple linear model for health trajectories given baseline data,

$$\begin{aligned}y_{t_k, i} &= y_{t_0, i} + \beta(\mathbf{y}_{t_0}, \mathbf{u}_{t_0}, t_0)(t_k - t_0), \\ \beta_i(\mathbf{y}_{t_0}, \mathbf{u}_{t_0}, t_0) &= \beta_{0, i} t_0 + \boldsymbol{\beta}_{1, i} \cdot \mathbf{y}_{t_0} + \boldsymbol{\beta}_{2, i} \cdot \mathbf{u}_{t_0},\end{aligned}\tag{25}$$

trained independently for each variable i . The parameters $\beta_{0, i}$, $\boldsymbol{\beta}_{1, i}$, and $\boldsymbol{\beta}_{2, i}$ are trained with elastic net regularization.

4. Linear models' hyperparameters

We perform a random search over the L_1 and L_2 elastic net regularization parameters and the MICE random forest maximum depth using the validation set. The regularization term in the elastic net models is $\alpha l_{1, ratio} \|\beta\|_1 + \frac{1}{2} \alpha (1 - l_{1, ratio}) \|\beta\|_2^2$, the common form of elastic net regularization used in Scikit-learn [69], the package we use to implement the elastic net linear model. We do the random search over $\log_{10} \alpha \in [-4, 0]$, $\log_{10} l_{1, ratio} \in [-2, 0]$, and maximum tree depth in [5, 10] for 25 iterations.

We find the parameters $\alpha = 0.40423$, $l_{1, ratio} = 0.55942$, and a maximum tree depth of 10 for the longitudinal model hyperparameters. We find the parameters $\alpha = 0.00016$, $l_{1, ratio} = 0.15613$, and a maximum tree depth of 10 for the survival model hyperparameters.

I. Data availability

The English Longitudinal Study of Aging waves 0-8, 1998-2017 with identifier UKDA-SN-5050-17 is available at <https://www.elsa-project.ac.uk/accessing-elsa-data>. This requires registering with the UK Data Service.

J. Code availability

Our code is available at <https://github.com/Spencerfar/djin-aging>.

Supplemental Information for: Interpretable machine learning for high-dimensional trajectories of aging health

Spencer Farrell, Arnold Mitnitski, Kenneth Rockwood, and Andrew Rutenberg

I. DERIVING THE VARIATIONAL LOSS

We denote health variables observed at age t_k by \mathbf{y}_{t_k} , the background information at baseline by \mathbf{u}_{t_0} , the model health variable predictions by $\mathbf{x}(t_k)$, the latent variables for imputation/generation by \mathbf{z} , the age of death or last censoring age by a , the censoring indicator by c , parameters by $\boldsymbol{\theta}$, and variational parameters by $\boldsymbol{\phi}$.

To fit the model, we minimize the KL-divergence between the approximate posterior and the true posterior. This is equivalent to maximizing a lower bound to the model evidence. Starting with the model evidence,

$$\begin{aligned}
& \log p(\{\mathbf{y}_{t_k}\}_k | \mathbf{u}_{t_0}, \{\mathbf{o}_{t_k}\}_k, a, c) \\
&= \log \int d\boldsymbol{\theta} d\mathbf{z} d\mathbf{x}_0 dt p(\boldsymbol{\theta}) p(\mathbf{z}) p(\mathbf{x}_0 | \mathbf{z}, \mathbf{u}_{t_0}, t_0) p(\mathbf{x}(t) | \mathbf{x}_0, \mathbf{u}_{t_0}, t) p(a, c | \mathbf{x}(t), \mathbf{u}_{t_0}, t) \prod_k p(\mathbf{y}_{t_k} | \mathbf{x}(t_k), \mathbf{o}_{t_k}) \\
&= \log \int d\boldsymbol{\theta} d\mathbf{z} p(\boldsymbol{\theta}) p(\mathbf{z}) \int d\mathbf{x}_0 p(\mathbf{x}_0 | \mathbf{z}, \mathbf{u}_{t_0}, t_0) \int dt p(\mathbf{x}(t) | \mathbf{x}_0, \mathbf{u}_{t_0}, t) p(a, c | \mathbf{x}(t), \mathbf{u}_{t_0}, t) \prod_k p(\mathbf{y}_{t_k} | \mathbf{x}(t_k), \mathbf{o}_{t_k}) \\
&= \log \int d\boldsymbol{\theta} d\mathbf{z} p(\boldsymbol{\theta}) p(\mathbf{z}) \frac{q(\mathbf{z} | \mathbf{y}_{t_0}, \mathbf{u}_{t_0}, \mathbf{o}_{t_0}, t_0) q(\boldsymbol{\theta})}{q(\mathbf{z} | \mathbf{y}_{t_0}, \mathbf{u}_{t_0}, \mathbf{o}_{t_0}, t_0) q(\boldsymbol{\theta})} \int d\mathbf{x}_0 p(\mathbf{x}_0 | \mathbf{z}, \mathbf{u}_{t_0}, t_0) \int dt p(\mathbf{x}(t) | \mathbf{x}_0, \mathbf{u}_{t_0}, t) \frac{q(\mathbf{x}(t) | \mathbf{x}_0, \mathbf{u}_{t_0}, t)}{q(\mathbf{x}(t) | \mathbf{x}_0, \mathbf{u}_{t_0}, t)} p(a, c | \mathbf{x}(t), \mathbf{u}_{t_0}, t) \\
&\times \prod_k p(\mathbf{y}_{t_k} | \mathbf{x}(t_k), \mathbf{o}_{t_k}) \\
&= \log \mathbb{E}_{\mathbf{z}, \boldsymbol{\theta} \sim q} \left[\frac{p(\mathbf{z})}{q(\mathbf{z} | \mathbf{y}_{t_0}, \mathbf{u}_{t_0}, \mathbf{o}_{t_0}, t_0)} \mathbb{E}_{\mathbf{x}_0 | \mathbf{z} \sim p, \mathbf{x}(t) | \mathbf{x}_0 \sim q} \left[\int_{t_0}^a \frac{p(\mathbf{x}(t) | \mathbf{x}_0, \mathbf{u}_{t_0}, t)}{q(\mathbf{x}(t) | \mathbf{x}_0, \mathbf{u}_{t_0}, t)} p(a, c | \mathbf{x}(t), \mathbf{u}_{t_0}, t) dt \prod_k p(\mathbf{y}_{t_k} | \mathbf{x}(t_k), \mathbf{o}_{t_k}) \right] \right],
\end{aligned} \tag{1}$$

where we have introduced the approximate posteriors q . Using Jensen's Inequality we move the logarithm into the expectations, and define this lower bound as the objective function,

$$\begin{aligned}
\mathcal{L}(\boldsymbol{\phi}) &= \mathbb{E}_{\boldsymbol{\theta}, \mathbf{z} \sim q, \mathbf{x}_0 | \mathbf{z} \sim p, \mathbf{x}(t) | \mathbf{x}_0 \sim q} \left[\int_{t_0}^a \log \frac{p(\boldsymbol{\theta}) p(\mathbf{z}) p(\mathbf{x}(t) | \mathbf{x}_0, \mathbf{u}_{t_0}, t) p(\mathbf{y}_t | \mathbf{x}(t), \mathbf{o}_{t_k}) p(a, c | \mathbf{x}(t), \mathbf{u}_{t_0}, t)}{q(\mathbf{z} | \mathbf{y}_{t_0}, \mathbf{u}_{t_0}, \mathbf{o}_{t_0}, t_0) q(\boldsymbol{\theta}) q(\mathbf{x}(t) | \mathbf{x}_0, \mathbf{u}_{t_0}, t)} dt \right] \\
&= \mathbb{E} \left[\sum_k \log p(\mathbf{y}_{t_k} | \mathbf{x}(t_k), \mathbf{o}_{t_k}) + \int_{t_0}^a \left\{ \log p(a, c | \mathbf{x}(t), \mathbf{u}_{t_0}, t) + \log p(\mathbf{x}(t) | \mathbf{x}_0, \mathbf{u}_{t_0}, t) - \log q(\mathbf{x}(t) | \mathbf{x}_0, \mathbf{u}_{t_0}, t) \right\} dt \right] \\
&- KL(q(\boldsymbol{\theta}) || p(\boldsymbol{\theta})) - KL(q(\mathbf{z} | \mathbf{y}_{t_0}, \mathbf{u}_{t_0}, \mathbf{o}_{t_0}, t_0) || p(\mathbf{z})) \\
&= \mathbb{E} \left[\sum_k \mathbf{o}_{t_k} \odot \log \mathcal{N}(\mathbf{y}_{t_k} | \mathbf{x}(t_k), \boldsymbol{\sigma}_y) + \int_{t_0}^a \left\{ c \log S(a | \mathbf{x}(t), \mathbf{u}_{t_0}, t) + (1 - c) [\log \lambda(a | \mathbf{x}(t), \mathbf{u}_{t_0}, t) + \log S(a | \mathbf{x}(t), \mathbf{u}_{t_0}, t)] \right\} dt \right] \\
&- \frac{1}{2} \int_{t_0}^a \left\| \boldsymbol{\sigma}_x^{-1} \odot (\mathbf{W}\mathbf{x} + \mathbf{f}(\mathbf{x}(t), \mathbf{u}_{t_0}, t) - \mathbf{g}(\mathbf{x}(t), \mathbf{u}_{t_0}, t)) \right\|^2 dt \right] - KL(q(\boldsymbol{\theta}) || p(\boldsymbol{\theta})) - KL(q(\mathbf{z} | \mathbf{y}_{t_0}, \mathbf{u}_{t_0}, \mathbf{o}_{t_0}, t_0) || p(\mathbf{z})).
\end{aligned} \tag{2}$$

Plugging in the normalizing flows for the posterior of \mathbf{z} ,

$$\begin{aligned}
\mathcal{L}(\boldsymbol{\phi}) &= \mathbb{E} \left[\sum_k \mathbf{o}_{t_k} \odot \log \mathcal{N}(\mathbf{y}_{t_k} | \mathbf{x}(t_k), \boldsymbol{\sigma}_y) + \int_{t_0}^a \left\{ c \log S(a | \mathbf{x}(t), \mathbf{u}_{t_0}, t) + (1 - c) [\log \lambda(a | \mathbf{x}(t), \mathbf{u}_{t_0}, t) + \log S(a | \mathbf{x}(t), \mathbf{u}_{t_0}, t)] \right\} dt \right] \\
&- \frac{1}{2} \int_{t_0}^a \left\| \boldsymbol{\sigma}_x^{-1} \odot (\mathbf{W}\mathbf{x} + \mathbf{f}(\mathbf{x}(t), \mathbf{u}_{t_0}, t) - \mathbf{g}(\mathbf{x}(t), \mathbf{u}_{t_0}, t)) \right\|^2 dt \right] - KL(q(\boldsymbol{\theta}) || p(\boldsymbol{\theta})) - KL(q(\mathbf{z}^{(0)} | \mathbf{y}_{t_0}, \mathbf{u}_{t_0}, \mathbf{o}_{t_0}, t_0) || p(\mathbf{z}^{(0)})) \\
&+ \sum_{l=1}^L \log \left| \det \frac{\partial a^{(l)}(\mathbf{z}^{(l)}, \boldsymbol{\gamma}_z, \boldsymbol{\phi}_z)}{\partial \mathbf{z}^{(l)}} \right|.
\end{aligned}$$

Here we do not show the variational parameters $\boldsymbol{\phi}$ in the notation for the approximate posteriors q and the parameters $\boldsymbol{\theta}$ from the conditional distributions for simplicity. Additionally, we have averaged over the imputed or generated \mathbf{x}_0 . This is the objective function used in the methods.

II. ALTERNATE MODELS

A. Full neural network drift function and one-dimensional summary models

We compare our pair-wise interactions network model with two alternate models, where we directly incorporate dynamics for the latent state $\mathbf{z}(t)$ and apply the decoder to estimate the health variables $\mathbf{x}(t)$ at specific ages. With this approach we do not need to impute the baseline state of health variables, or to directly include dynamics for the baseline health. Rather a decoder directly maps the latent states $\mathbf{z}(t)$ to the predicted output of the health variables \mathbf{y}_t . This approach has the form,

$$\mathbf{z}_0, \boldsymbol{\theta} \sim p(\mathbf{z}_0)p(\boldsymbol{\theta}) \quad (\text{Prior})$$

$$d\mathbf{z}(t) = \mathbf{f}(\mathbf{z}(t), \mathbf{u}_{t_0}, t; \boldsymbol{\theta}_f) + \boldsymbol{\sigma}_z(\mathbf{z}(t))d\mathbf{B}(t), \mathbf{z}(t_0) = \mathbf{z}_0, \quad (\text{Dynamics})$$

$$S(t) = \exp\left(-\int_{t_0}^t \lambda(\{\mathbf{z}(\tau)\}_{\tau \leq t'}, \mathbf{u}_{t_0}, t'; \boldsymbol{\theta}_\lambda) dt'\right), \quad (\text{Survival})$$

$$\mathbf{y}_t \sim \mathcal{N}\left(\boldsymbol{\psi}^{-1}(\boldsymbol{\mu}(\mathbf{z}(t), \mathbf{u}_{t_0}, \mathbf{o}_{t_0}, \boldsymbol{\theta}_p)), \text{diag}(\sigma_{\mathbf{y}}^2)\right), \quad (\text{Health observation})$$

$$a \sim \lambda(\{\mathbf{z}(\tau)\}_{\tau \leq a}, \mathbf{u}_{t_0}, a; \boldsymbol{\theta}_\lambda)S(a), \quad (\text{Survival observation})$$

$$p(\{\mathbf{z}(t)\}_t, \boldsymbol{\theta} | \{\mathbf{y}_{t_k}\}_k, \mathbf{u}_{t_0}, t_0, a, c) \propto p(\boldsymbol{\theta})p(\mathbf{z}_0)p(\{\mathbf{z}(t)\}_t | \mathbf{z}_0, \mathbf{u}_{t_0}, t, \boldsymbol{\theta}) \times \quad (\text{Inference})$$

$$p(a, c | \{\mathbf{z}(t)\}_t, \mathbf{u}_{t_0}, t, \boldsymbol{\theta}) \prod_k p(\mathbf{y}_{t_k} | \{\mathbf{z}(t_k)\}_k, \boldsymbol{\theta}),$$

$$\boldsymbol{\theta} = \{\mathbf{W}, \sigma_{\mathbf{y}}, \sigma_{\mathbf{x}}, \boldsymbol{\theta}_\lambda, \boldsymbol{\theta}_p, \boldsymbol{\theta}_f\}, \quad (\text{Parameters})$$

where instead of the variable-wise neural networks in the pair-wise network model, the function \mathbf{f} is now a full neural network including the interactions of all variables. The function $\boldsymbol{\mu}$ is a decoder neural network which outputs the mean of a Gaussian distribution for the health variables \mathbf{y}_t , from the latent state at that age.

For the full neural network model, we set the dimension of \mathbf{z} to be $N + 1$. For a second alternative model we use a dimension of 1 – which leads to one-dimensional dynamics for a summary health-variable. Additionally for the one-dimensional model, we only use the sex, ethnicity, and country of birth components of \mathbf{u}_{t_0} for the drift functions \mathbf{f} and \mathbf{g} and the mortality rate λ . This is because the other components contain additional health information that should be included in the one-dimensional summary health measure.

All hyperparameters remain the same from these alternate models and the pair-wise network model. In particular, the form of the loss function remains the same, except that the priors for \mathbf{W} are removed, and the form of the drift function in the SDE is adjusted. The neural network parameters for these alternative models are trained with the loss function using the same approach as our primary DJIN model.

B. Non-recurrent neural network mortality rate

In our network model presented in the main results, we model the mortality rate with a recurrent neural network (RNN). This allows the use of a history of health to compute the mortality rate. We have also tested a model where we instead use a feed-forward neural network taking $\mathbf{x}(t), \mathbf{u}_{t_0}, t$ as input – this allows no memory of previous states to determine mortality. We use the same layer sizes as the recurrent neural network model, and use ELU activations.

III. GENERATED SYNTHETIC POPULATION

We have made a synthetic population available at <https://zenodo.org/record/4733386>. This population includes 3 million individuals for each baseline age of 65, 75, and 85 years old, for a total of 9 million individuals. The background health state has been generated by sampling based on the age and sex-dependent ELSA population. For binary variables we sample a 0 or 1 based on the observed sex and age-dependent prevalence, for continuous variables we sample from a Gaussian distribution with mean and standard deviation from the observed sex and age-dependent population mean and standard deviation. We set all individuals with no medications.

Using this input, we sample a baseline state for each synthetic individual and simulate their health trajectories for 20 years.

IV. SUPPLEMENTAL FIGURES

In Fig. S1 we show the variables used in the ELSA data set, and the number of individuals for which each variable is observed at each year from baseline. The shaded fills indicate the proportion of observed variables (with respect to the maximum of that variable), with the darkest fill indicating almost 100%. Most variables are unobserved after baseline, and many are unobserved at baseline – which reinforces the need for effective baseline imputation. The full names of these variables are provided in supplemental Table I.

In Fig. S2, we show the relative RMSE of our model predictions and the elastic net linear model predictions for each health variable between 1 and 6 years – plotted against the proportion of observations for which the variable is missing in the full dataset. Our model predictions are generally worse for the variables with a higher proportion missing, with observable degradation for proportions of missing around 0.95 where accuracy goes above the population mean predictions, although our model is always better than the elastic net linear model.

In Fig. S3 we show 3 different example individuals from the test set and the model predicted trajectories. We choose the 6 of the best predicted variables to show. These predictions show the estimated uncertainty for these individual trajectories, and the variety in behaviour in the data for different individuals. The relative RMSE for these individuals averaged over each time point is shown, for comparison with Fig. 2 in the main results.

In Fig. S4 we show the generated synthetic population Kaplan-Meier survival curve (red line and shading) and the observed population Kaplan-Meier survival curve (blue line and shading) with 95% confidence intervals indicated by the shading. The same censoring distribution seen in the observed population is applied to the synthetic population by sampling censoring ages above the baseline age from the test data with replacement. Agreement is good until ~ 90 years, after which the number of individuals observed in the dataset is very low.

In Fig. S5 we show the classification accuracy for a logistic regression model discriminating between the synthetic and observed populations. Our model generated a synthetic population that is almost indistinguishable from the observed population for most individuals, only rising to 60% accuracy at 18 years from baseline.

In Fig. S6 we show the one-dimensional marginal distributions for each health variable for the generated synthetic population and observed population at baseline. We see the synthetic population agrees with the observed population, but often has a slightly lower variance. In Fig. S7 we show the mean and standard deviation of generated synthetic population trajectories (red lines and shading) and the observed population trajectories (blue lines and shading). The synthetic trajectories have somewhat lower variance but reasonable agreement with the means.

In Fig. S8, we contrast our network model’s weight matrix with a pair-wise Pearson correlation network, where weights have been pruned with a p-value above 0.01 to match the 99% credible intervals used in our approach. We see many differences. Our weight matrix is much more sparse, including only the links useful for prediction. Our network is also directed and asymmetric, and one-way links between variables are observed, as well as distinct strengths of links in the different directions. However, the sign of the links in the weight matrix is typically the same as in the correlation network.

In Fig. S9 we show, for each network weight, the posterior mean of the weight vs. the proportion of the approximate posterior distribution that is above zero for posterior weights, or below zero for negative weights. We exclude weights when the probability of the weight being in the opposite direction of the mean is above 1%. This approach only accepts connections with a large probability of having a definite sign. We see that large weights only have a small proportion of the posterior with the opposite sign; showing that the strong connections inferred by the model are robust.

Several alternative models were explored, as described in Supplemental Sec. II. In Fig. S10 we summarize predictions for the one-dimensional summary model, in which dynamics are built on one latent summary health variable. This model performs worse than our DJIN model for both health and survival, and is often even worse than a static baseline prediction model (blue squares) for health. In Fig. S11 we show model results with a full neural network drift function that includes all interactions, in contrast to the linear pair-wise network in our main results with the DJIN model. This shows that the full NN model only does slightly better than the pair-wise network model for health, and is slightly worse for survival. This indicates that the pair-wise network assumptions made by our DJIN model do not sacrifice much accuracy. In Fig. S12 we show the model results with a feed-forward neural network for the mortality rate instead of a recurrent neural network (GRU). Our recurrent neural network (RNN) model achieves slightly better C-index and Brier scores, particularly for older ages. The models are nearly equivalent for longitudinal prediction.

In Fig. S13 we show the D-calibration histogram comparison between the DJIN model and the elastic net Cox model. The histograms reflect the χ^2 and p-values given in the main results, showing that the both models have calibrated probabilities.

		Number of individuals with measurements																						
		0	1	2	3	4	5	6	7	8	9	10	11	12	13	14	15	16	17	18	19	20	21	22
Health variables	Gait speed	1426	1838	1969	2409	4901	2445	3861	3006	4129	2468	3006	2785	2487	2444	2323	2027	2005	931	1284	458	4	1	2
	Dom grip str	2649	24	634	1951	3196	685	3328	2578	1128	591	2243	2331	659	595	1650	1144	383	259	830	290	1	0	0
	Ndom grip str	2643	24	632	1951	3193	682	3330	2569	1129	585	2237	2308	660	595	1649	1142	383	260	833	292	1	0	0
	ADL score	6144	3354	3756	4631	8994	4140	6794	4625	6092	1856	3044	2877	1019	2208	2884	2505	2435	1140	1526	557	5	2	2
	IADL score	6144	3354	3756	4631	8995	4141	6793	4625	6091	1856	3044	2878	1019	2207	2884	2507	2435	1140	1526	558	5	2	2
	5 Chair rises	2334	20	569	1684	2380	530	2840	2170	902	450	1592	1888	560	496	1304	448	1	0	1	0	0	0	0
	Leg raise	676	5	146	459	623	145	783	591	237	105	374	447	126	107	286	104	0	0	1	0	0	0	0
	Full tandem	315	3	45	303	389	112	466	351	169	85	312	348	108	95	254	79	0	0	1	0	0	0	0
	Self-rated health	25347	2018	4674	3672	7360	3966	6603	4532	6042	3320	3941	3472	3086	2931	2735	2367	2322	1076	1454	523	5	1	2
	Eyesight	6289	3681	5624	4780	9964	4366	6820	4637	6239	3452	4095	3626	3267	3113	2891	2508	2435	1138	1526	557	5	2	2
	Hearing	6290	3680	5624	4781	9966	4367	6822	4636	6240	3452	4097	3624	3268	3113	2892	2509	2437	1139	1526	557	5	2	2
	Walking ability	6251	3645	5602	4754	9912	4357	6819	4637	6242	3449	4096	3627	3269	3113	2893	2509	2436	1140	1526	557	5	2	2
	Dias BP	16270	24	636	1981	3222	687	3368	2606	1144	603	2272	2363	674	619	1698	1170	386	270	861	296	1	0	0
	Sys BP	16270	24	636	1982	3222	686	3368	2606	1144	603	2272	2363	674	619	1698	1170	386	270	861	296	1	0	0
	Pulse	16269	24	636	1981	3221	686	3367	2606	1144	603	2271	2362	674	619	1698	1170	386	270	861	296	1	0	0
	Trig	2380	17	492	1506	2540	555	2670	1992	862	450	1742	1779	514	471	1263	876	283	207	643	230	1	0	0
	C-RP	8239	17	492	1506	2540	554	2666	1990	863	450	1743	1779	514	472	1263	876	283	207	644	230	1	0	0
	HDL	8045	17	491	1505	2538	555	2669	1990	863	450	1738	1779	514	471	1263	876	283	207	643	230	1	0	0
	LDL	2307	17	473	1476	2487	539	2599	1948	844	443	1701	1744	513	467	1253	866	279	206	639	228	1	0	0
	Gluc	1614	11	315	872	1524	317	1560	1160	496	279	1031	1003	260	247	626	471	142	100	336	125	0	0	0
	IGF-1	2069	17	448	1480	1288	136	551	947	829	441	1725	1774	513	467	1262	875	283	206	642	230	1	0	0
	Hgb	8168	17	487	1492	2515	548	2631	1961	851	439	1724	1759	511	465	1241	863	275	205	634	228	1	0	0
Fibr	7322	17	488	1489	2483	543	2646	1949	831	437	1681	1745	499	467	1226	799	256	183	575	207	1	0	0	
Ferr	8091	17	492	1507	2540	555	2671	1991	863	450	1743	1779	514	471	1263	876	283	206	642	230	1	0	0	
Total chol	2448	17	492	1506	2540	555	2670	1992	863	450	1742	1779	514	471	1263	876	283	207	643	230	1	0	0	
WBC	2056	17	448	1483	1280	135	537	933	828	438	1726	1760	511	465	1241	863	275	205	634	228	1	0	0	
MCH	2055	17	448	1483	1280	135	537	933	828	438	1726	1760	511	465	1241	863	275	205	634	228	1	0	0	
HgbA1C	2444	16	488	1492	2501	544	2620	1973	854	440	1722	1759	511	466	1240	860	272	205	631	227	1	0	0	
Vit-D	609	0	19	294	1280	131	479	84	45	36	371	1011	489	467	1262	872	282	203	638	229	1	0	0	
Background	Longterm ill	26066	3680	5623	4780	9965	4364	6822	4636	6242	3450	4097	3627	3268	3113	2892	2507	2437	1140	1526	557	5	2	2
	Illness limits	14520	2026	2749	2690	5312	2378	3753	2643	3472	1986	2250	2097	1882	1846	1700	1523	1461	661	914	338	4	1	1
	Everythings effort	5846	3581	5247	4637	9575	4212	6558	4515	6013	3288	3914	3452	3061	2912	2719	2345	2304	1067	1448	519	5	1	2
	Ever smoke	25713	3425	2686	2312	5885	957	937	281	835	728	747	928	1187	1107	1034	845	847	391	529	184	1	1	0
	Smoke now	25868	3644	5511	4753	9887	4350	6813	4621	6229	3417	4054	3599	3222	3094	2891	2502	2436	1137	1522	557	5	2	2
	Height	22064	3468	4133	4590	9085	4232	6447	4578	5974	3431	4004	3594	3262	3109	2889	2491	2424	1134	1521	556	5	1	2
	BMI	20453	24	621	1911	2775	600	3256	2513	1067	546	1897	2233	651	594	1588	536	1	0	1	0	0	0	0
	Mobility	1522	1982	2107	2610	5268	2612	4140	3198	4399	2630	3225	2994	2685	2645	2523	2195	2168	1015	1373	486	4	1	2
	Country	13658	3658	5597	3600	7156	3557	5031	3418	4933	2801	3247	2981	2503	2613	2358	2236	2158	1053	1525	558	5	2	2
	Alcohol	4918	3598	4862	4374	9136	3711	5792	3959	5251	2903	3477	3075	2786	2627	2422	2109	2062	965	1313	461	3	1	2
	Joint replace	1713	2090	2350	2784	5548	2797	4430	3396	4728	2862	3477	3235	2971	2930	2779	2429	2374	1113	1496	546	5	2	2
	Fractures	1682	2068	2322	2742	5506	2779	4402	3393	4728	2863	3477	3234	2970	2930	2778	2429	2374	1112	1496	546	5	2	2
	Sex	26078	3684	5651	4875	10035	4468	6997	4718	6347	3545	4193	3676	3321	3146	2921	2514	2439	1140	1526	558	5	2	2
	Ethnicity	26078	3684	5651	4875	10035	4468	6997	4718	6347	3545	4193	3676	3321	3146	2921	2514	2439	1140	1526	558	5	2	2
	Blood pres med	11131	1330	1811	1502	3282	1619	2181	1749	2704	1562	1837	1647	1567	1454	1380	1182	1156	563	723	273	2	1	1
	Blood thin med	404	53	406	166	320	348	443	632	780	690	805	581	596	363	275	195	193	106	107	49	0	0	0
	Chol med	10022	123	1082	284	1047	877	1076	1072	2050	1213	1468	1324	1264	1177	1091	976	953	469	598	221	1	1	1
	Hipknee med	200	20	234	169	445	202	344	329	549	247	373	291	229	143	186	356	161	120	323	124	1	1	0
	Lung med	831	485	734	699	1271	640	1027	704	854	517	552	555	461	485	425	392	366	174	248	82	2	0	0
	Deaths	0	0	23	93	65	99	171	81	101	92	95	48	51	31	26	5	1	0	0	0	0	0	0
	Total individuals	26078	3684	5651	4875	10035	4468	6997	4718	6347	3545	4193	3676	3321	3146	2921	2514	2439	1140	1526	558	5	2	2

FIG. S1. **Coverage of ELSA dataset.** Number of individuals with measurements vs number of years after baseline. Health variables (purple shading) are included in \mathbf{y}_t . Background variables (green shading) are included in \mathbf{u}_{t_0} . Indicated at the bottom (orange shading) are the number of deaths reported, the number of individuals, and the average coverage percentage for those individuals. The darker shading indicates more measurements, relative to the maximum for that variable.

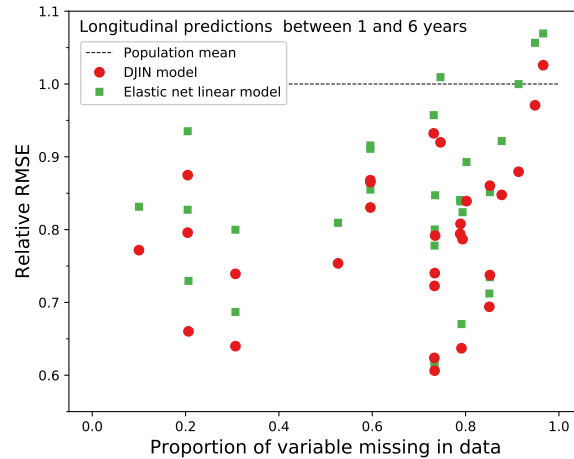


FIG. S2. **Longitudinal predictions vs proportion missing.** Relative RMSE up to six-years past baseline for longitudinal predictions of each health variable plotted against the proportion of observations where that variable was missing. Red circles show our network DJIN model, while green squares show the elastic net linear model. Predictions degrade only at high missingness.

TABLE I. Variables used from the ELSA dataset. Background variables are only used at the first time-step, as \mathbf{u}_{t_0} . Longitudinal variables are predicted in \mathbf{y}_t . All variables are z-scored; additional transformations before z-scoring are indicated.

Variable	Category	Wave type	Transformation
Gait speed (average of 3 measurements, speed over 8 feet)	Longitudinal	Nurse	
Dominant hand grip strength (average of 3 measurements)	Longitudinal	Nurse	
Non-dominant hand grip strength (average of 3 measurements)	Longitudinal	Nurse	
ADL score (count from 0-10)	Longitudinal	Self-report	
IADL score (count from 0-13)	Longitudinal	Self-report	
Time to rise from a chair 5x	Longitudinal	Nurse	
Time held leg raise (eyes open, maximum 30 secs)	Longitudinal	Nurse	Log-scaled
Time held full tandem stance (maximum 30 secs)	Longitudinal	Nurse	Log-scaled
Self-rated health (scored 0=excellent to 1=poor, 5 levels)	Longitudinal	Self-report	
Eyesight (with aids) (scored 0=excellent 1=legally blind, levels=6)	Longitudinal	Self-report	
Hearing (with aids) (scored 0=excellent to 1=poor, 5 levels)	Longitudinal	Self-report	
Walking ability score (unaided ability to walk 1/4 mile) (scored 0=no difficulty to 1=unable to do this, 4 levels)	Longitudinal	Self-report	
Diastolic blood pressure (average of 3 measurements)	Longitudinal	Nurse	
Systolic blood pressure (average of 3 measurements)	Longitudinal	Nurse	
Pulse (average of 3 measurements)	Longitudinal	Nurse	
Triglycerides	Longitudinal	Nurse	Log-scaled
C-reactive protein	Longitudinal	Nurse	Log-scaled
HDL cholesterol	Longitudinal	Nurse	
LDL cholesterol	Longitudinal	Nurse	
Glucose (fasting)	Longitudinal	Nurse	
Insulin-like growth factor 1	Longitudinal	Nurse	
Hemoglobin	Longitudinal	Nurse	
Fibrinogen	Longitudinal	Nurse	
Ferritin	Longitudinal	Nurse	Log-scaled
Total cholesterol	Longitudinal	Nurse	
White blood cell count	Longitudinal	Nurse	Log-scaled
Mean corpuscular haemoglobin	Longitudinal	Nurse	Log-scaled
Glycated hemoglobin (HgbA1c) (%)	Longitudinal	Nurse	
Vitamin-D	Longitudinal	Nurse	Log-scaled
Long-standing illness (yes/no)	Background	Self-report	
Long-standing illness limits activities (yes/no)	Background	Self-report	
Everything is an effort lately (yes/no)	Background	Self-report	
Ever smoked (yes/no)	Background	Self-report	
Currently smoke (yes/no)	Background	Self-report	
Height	Background	Nurse	
Body mass index (weight/height ²)	Background	Nurse	
Mobility status (mobile/immobile)	Background	Nurse	
Country of birth (UK/outside UK)	Background	Self-report	
Drink alcohol (last 12 months, scored 1=almost every day to 6=every couple of months)	Background	Self-report	
Ever had a joint replacement (yes/no)	Background	Self-report	
Ever had bone fractures (yes/no)	Background	Self-report	
Sex	Background	Self-report	
Ethnicity (white/non-white)	Background	Self-report	
Hypertension medication (yes/no)	Background	Self-report	
Anticoagulant medication (yes/no)	Background	Self-report	
Cholesterol medication (yes/no)	Background	Self-report	
Hip/knee treatment (medication or exercise, yes/no)	Background	Self-report	
Lung/asthma medication (yes/no)	Background	Self-report	

TABLE II. Neural network architectures used in the DJIN model, as described in Fig. 1 and Sec. III of the methods.

Encoder (VAE)	
Layer #	Description
1	Input ($\mathbf{y}_{t_0}, \mathbf{o}_{t_0}, \mathbf{u}, t_0$)
2	$(2N+B+1+17) \times 95$ Fully connected layer
3	Batchnorm
4	ELU
5	95×70 Fully connected layer
6	Batchnorm
7	ELU
8	70×50 Fully connected layer

Decoder (VAE)	
Layer #	Description
1	Input ($\mathbf{z}, \mathbf{u}_{t_0}, t_0$)
2	$(20+B+1+17) \times 65$ Fully connected layer
3	Batchnorm
4	ELU
5	$65 \times N$ Fully connected layer

Diagonal dynamics f_i	
Layer #	Layer description
1	Input ($x_i(t), t, \mathbf{u}_{t_0}$)
2	$(2+B+17) \times 12$ Fully connected layer
3	ELU
4	12×1 Fully connected layer

Mortality rate λ	
Layer #	Layer description
1	Input ($\mathbf{x}(t), t$)
2	$(N+1) \times 25$ GRU
3	25×10 GRU
4	ELU
5	10×1 Linear layer

Posterior drift function g	
Layer #	Layer description
1	Input ($\mathbf{x}(t), \mathbf{u}_{t_0}, t$)
2	$(N+B+1+17) \times 8$ Fully connected layer
3	ELU
4	$8 \times N$ Fully connected layer

Inferring \mathbf{h}_{t_0}	
Layer #	Layer description
1	Input ($\mathbf{x}(t_0), \mathbf{u}_{t_0}, t_0$)
2	$(N+B+1+17) \times 75$ Fully connected layer
3	ELU
4	75×40 Fully connected layer

Normalizing flow a	
Layer #	Layer description
1	Input ($\mathbf{z}^{(0)}, \gamma$)
2	30×24 Fully connected layer
3	BatchNorm
4	Tanh
5	24×20 Fully connected layer

Dynamical noise strength $\sigma_{\mathbf{x}}$	
Layer #	Layer description
1	Input ($\mathbf{x}(t)$)
2	$N \times N$ Fully connected layer
3	ELU
4	$N \times N$ Fully connected layer
5	Sigmoid

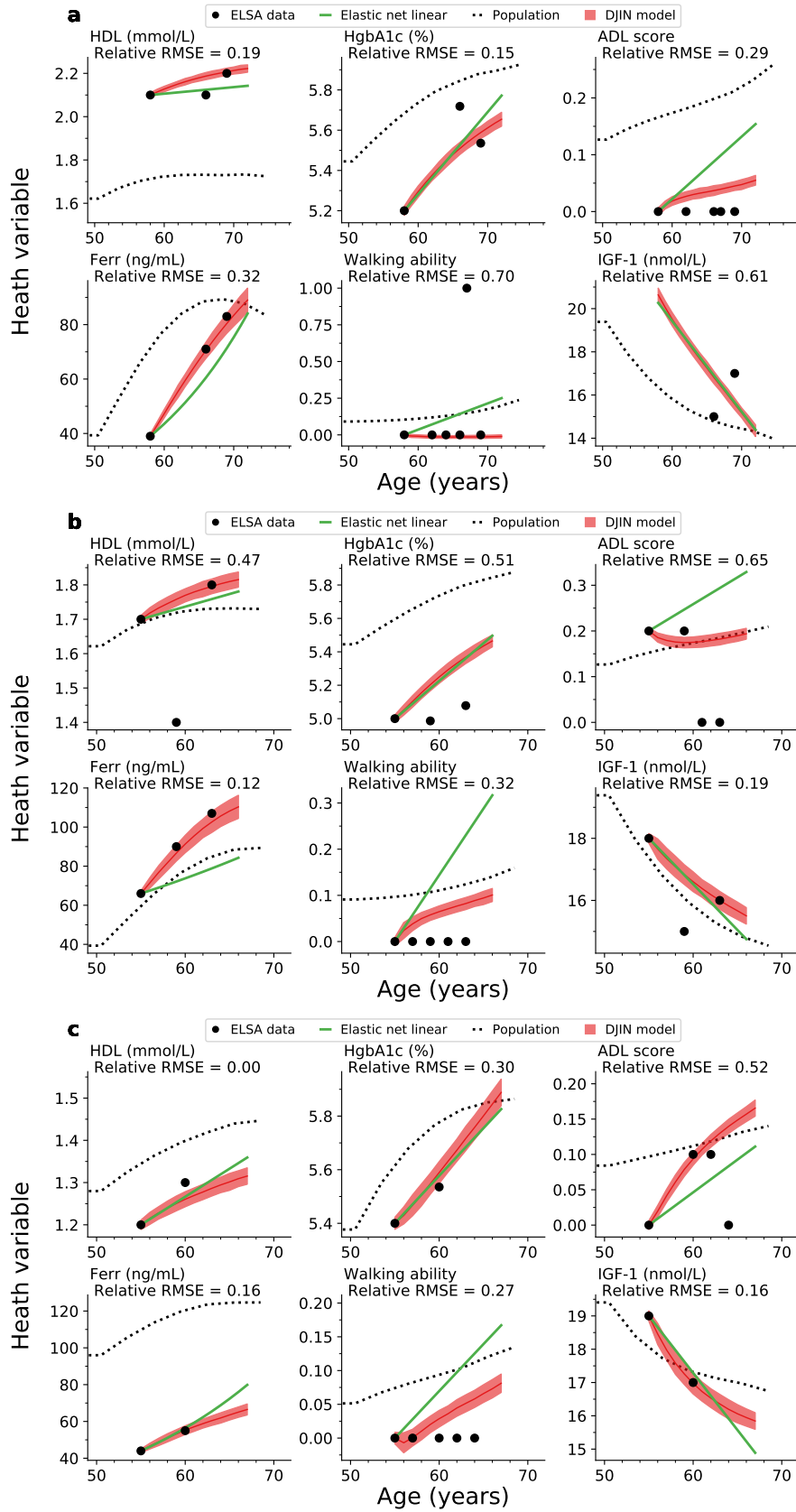


FIG. S3. **Model example trajectories.** We show example predictions for 3 test individuals (**a**, **b**, and **c**). For each individual we show the top 6 best predicted health variables from Figure 2 in the main results. Black circles show the observed ELSA data. Red lines indicate the mean predicted $\mathbf{x}(t)$ and the red shaded region is one standard deviation from the predicted mean trajectory. The average relative RMSE for each variable for each individual is shown.

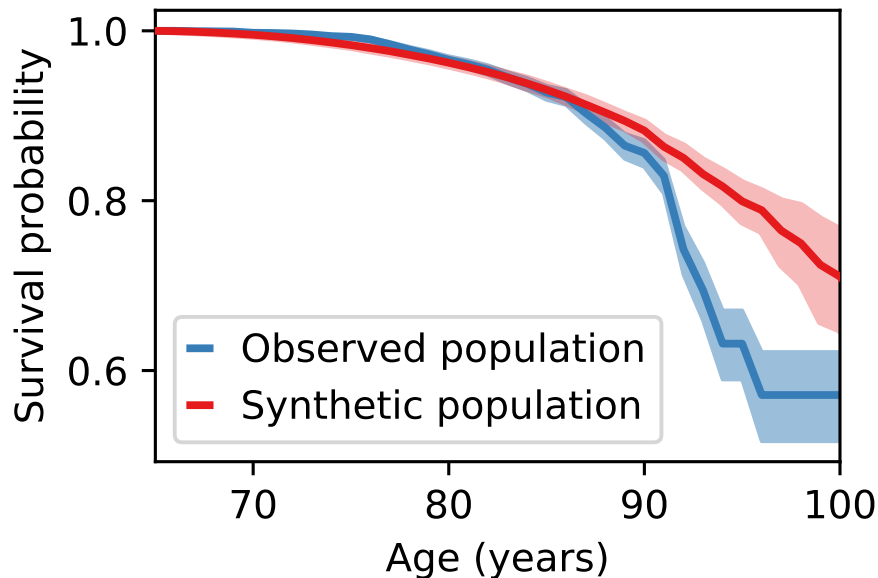


FIG. S4. **Synthetic survival distribution.** Survival curve for synthetic and observed populations, as indicated. The shaded regions show the 95% confidence intervals for Kaplan-Meier curves. The observed population censoring distribution is applied to the synthetic population. The survival probability is approximately the same until 90 years, indicating that the mortality of the synthetic population is representative until older ages.

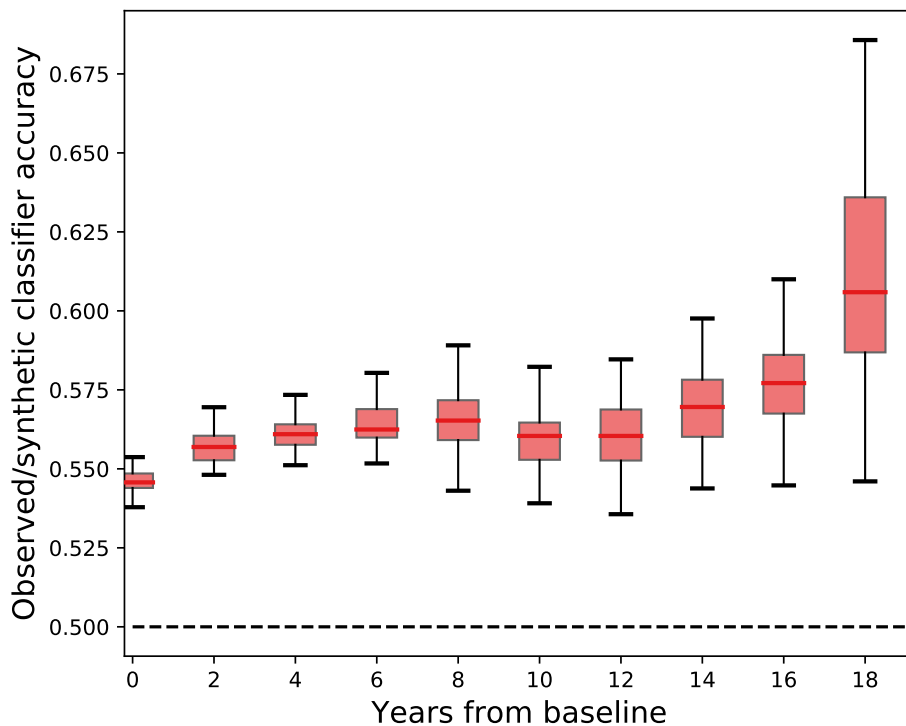


FIG. S5. **Synthetic population classification.** We use a logistic regression classifier to evaluate the quality of our synthetic population by the classifier's ability to differentiate the synthetic population from the observed population. The boxplot shows the median with the red line, interquartile range with the box, and 1.5x from the interquartile range as the whiskers. A completely indistinguishable population would have a classification accuracy of 0.5. We show the classification accuracy vs years from baseline, showing low classification accuracies that increase slowly with time from baseline.

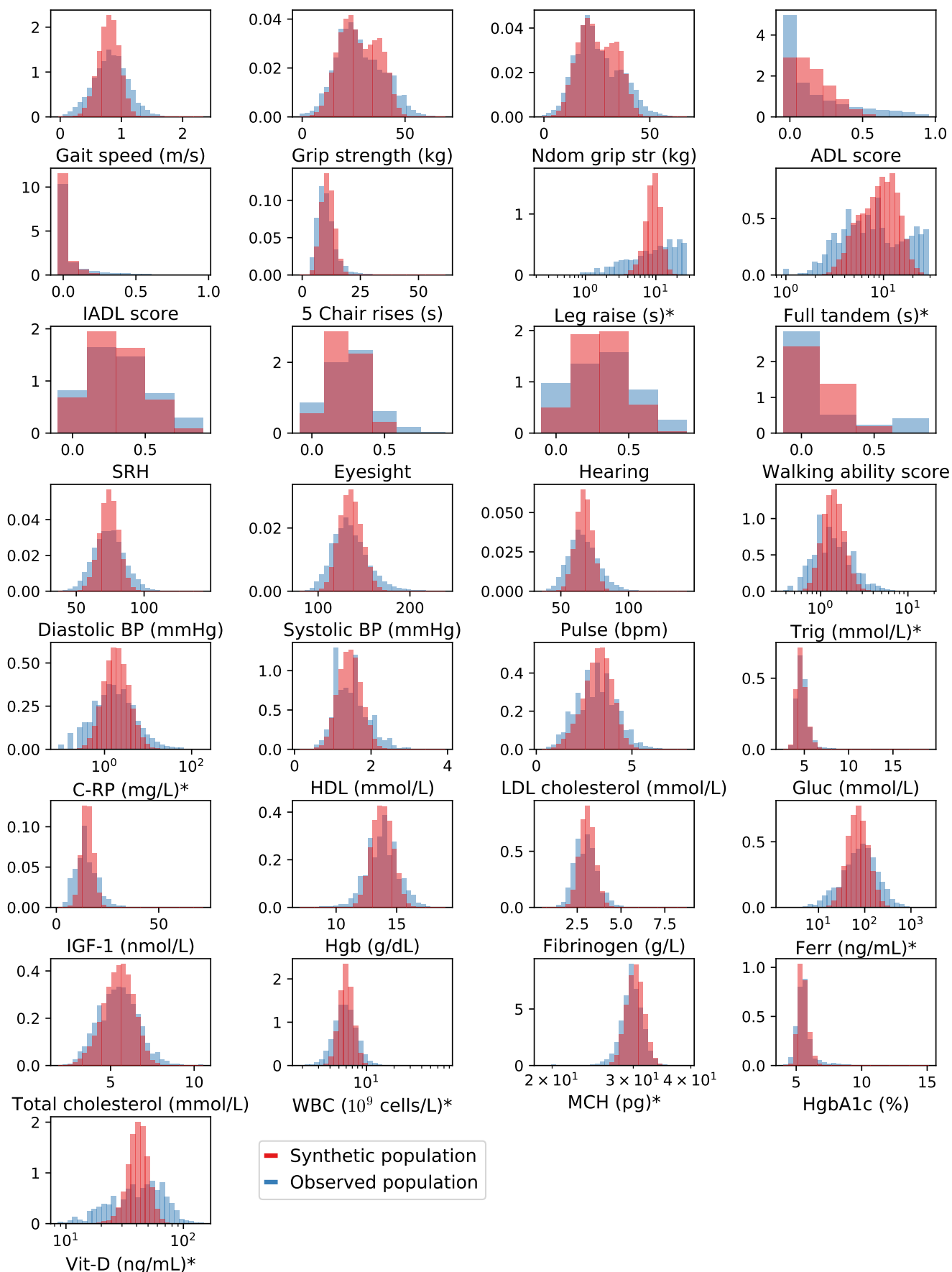


FIG. S6. **Synthetic population baseline distributions.** Each plot shows a synthetic baseline marginal distribution (red shading) for each variable. The synthetic baseline is generated given the background variables \mathbf{u}_{t_0} for the test set. Also shown is the observed population distribution (blue shading). Log-scaled variables are shown with a logarithmic x-axis, and are indicated with an *.

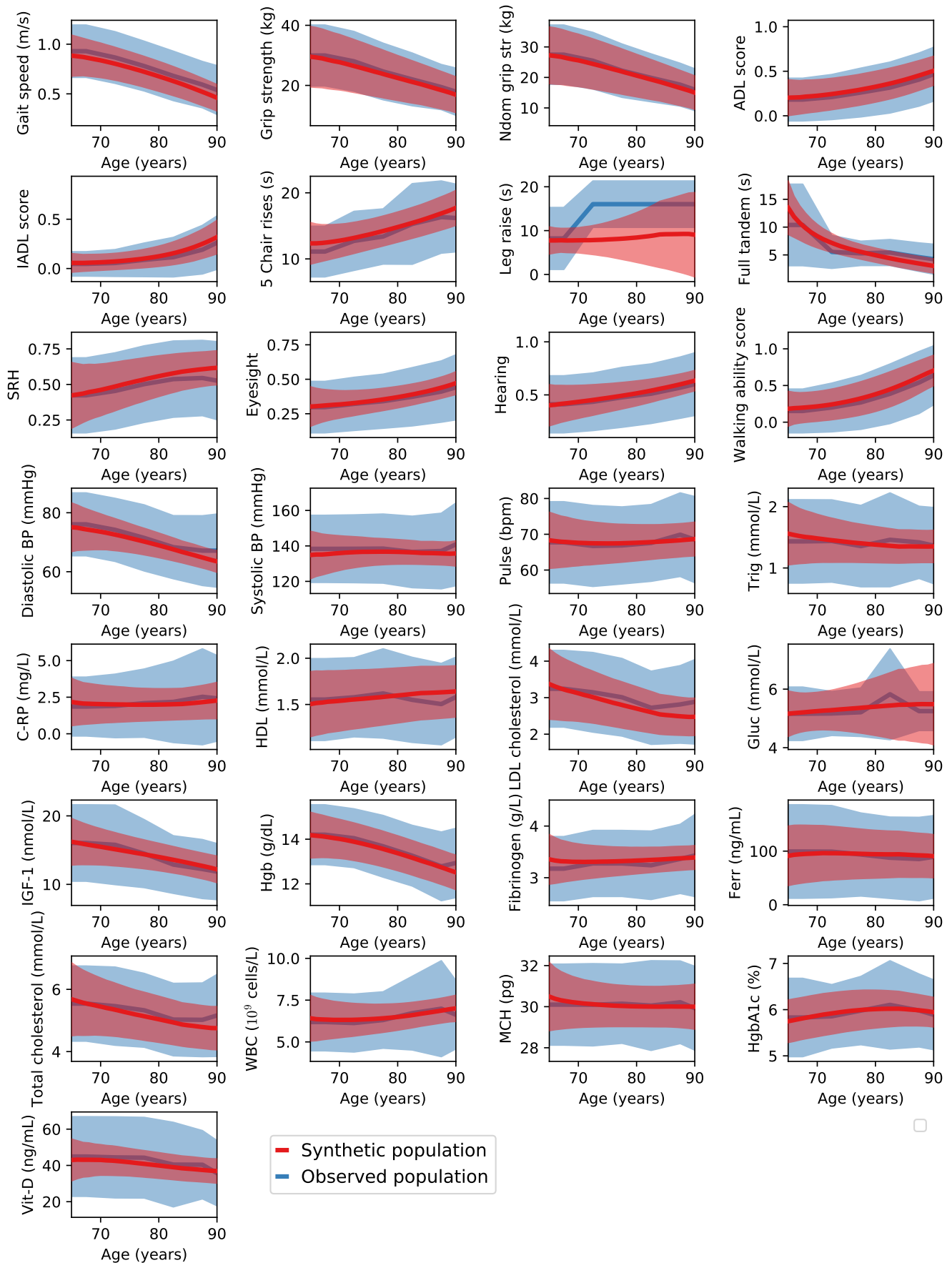


FIG. S7. **Synthetic population trajectories.** Red lines show the synthetic population trajectory marginal distribution means for each variable. Red shaded regions indicate 1 standard deviation away from the mean. Synthetic trajectories are generated from the baseline states shown in Fig. S6. Blue lines and shaded regions indicate the corresponding means and 1 standard deviation away for the observed population.

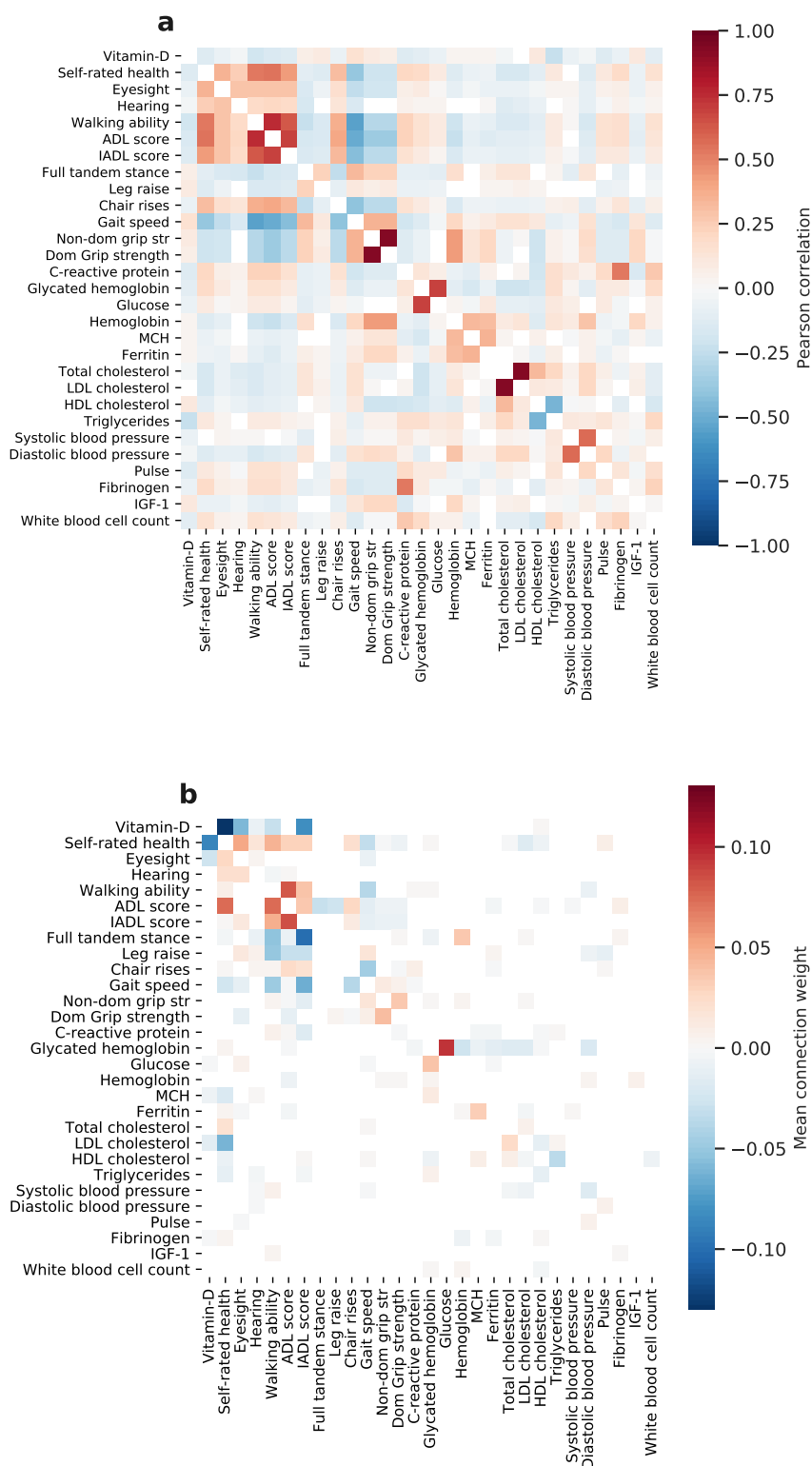


FIG. S8. **Comparison with correlation network.** **a)** Pearson correlation network between the health variables for all individuals at all time-points, values are pruned for p-values above 0.01. **b)** Our model interaction network. Weights are pruned when the 99% posterior credible interval includes zero.

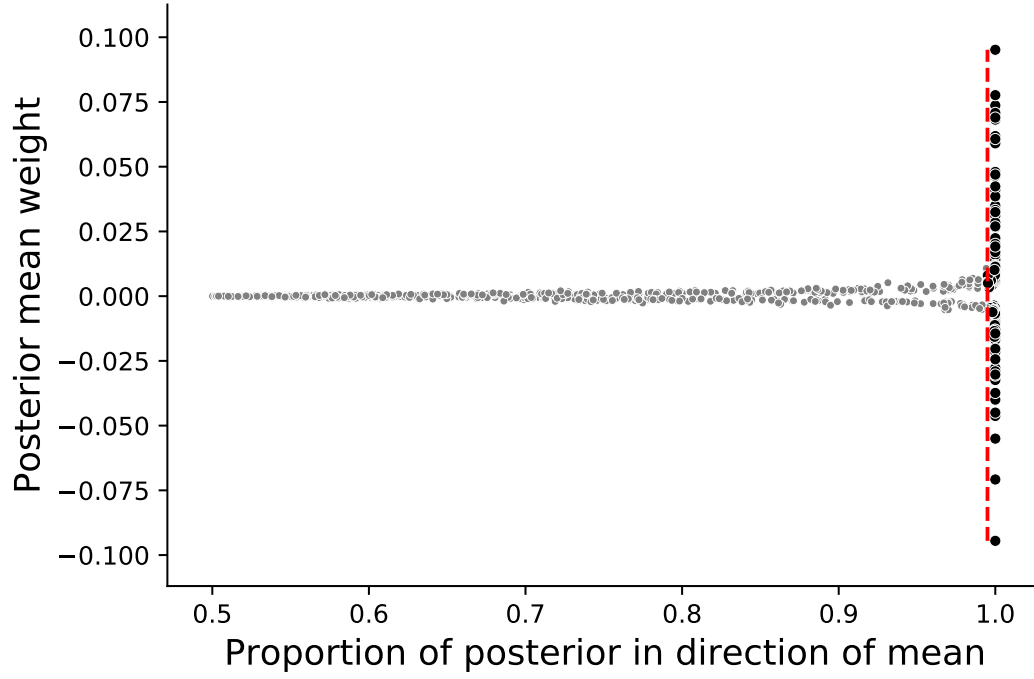


FIG. S9. **Network criterion.** Criteria for determining robust connections. We show the posterior mean of the network weights $\{W_{ij}\}$ vs. the proportion of the posterior above zero for weights with a positive mean, and below zero for weights with a negative mean. The vertical dashed red line shows the criteria for robust connections (shown in Fig. S8b), which is a 99% credible interval around the mean not containing zero. We see that larger weights are all credible, while many smaller weights are not.

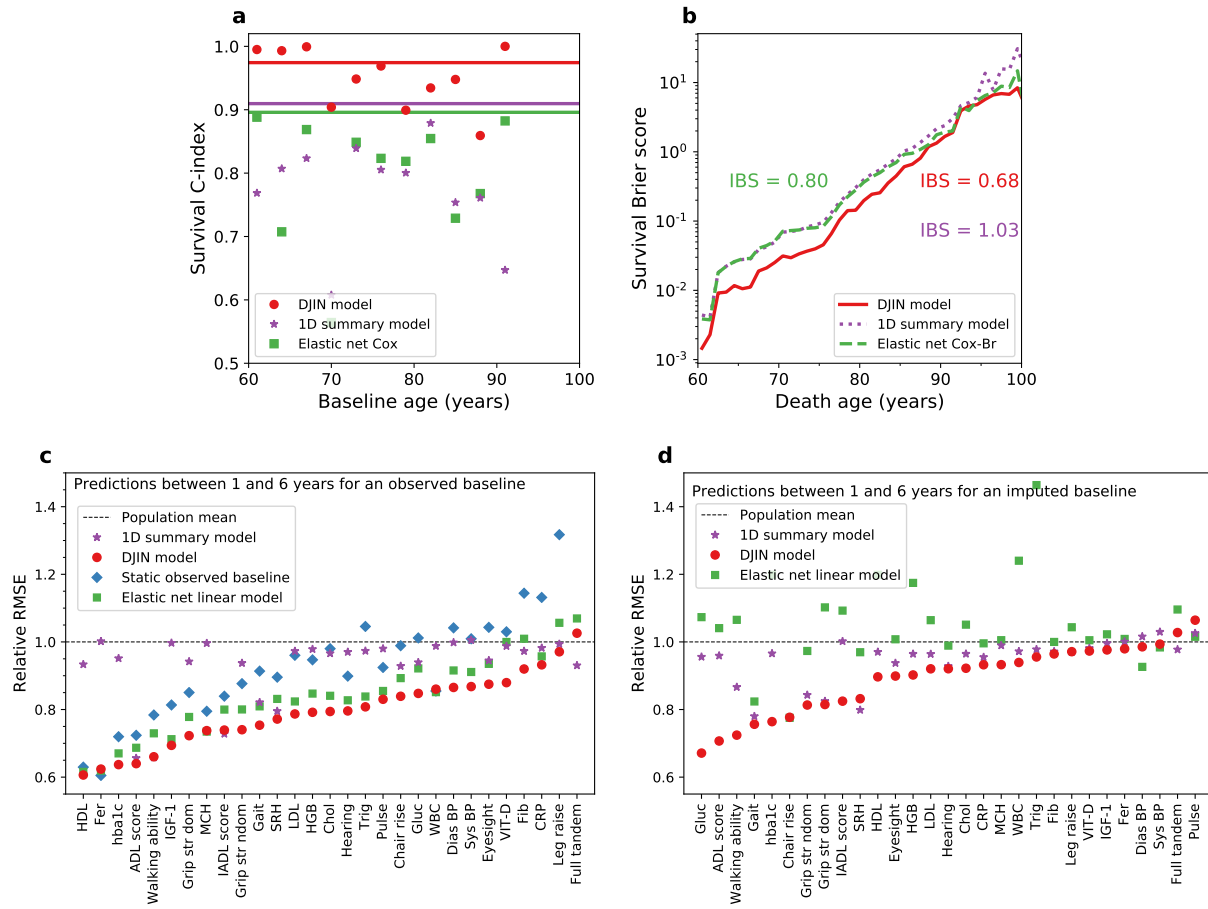


FIG. S10. **One-dimensional summary model.** **a)** Time-dependent C-index stratified vs age (points) and for all ages (line). Results are shown for the 1D summary model (purple), the DJIN network model shown in the main results (red) and a Elastic net Cox model (green). (Higher scores are better). **b)** Brier scores for the survival function vs death age. Integrated Brier scores (IBS) over the full range of death ages is also shown. (Lower scores are better). **c)** RMSE scores when the baseline value is observed for each health variable for predictions at least 5 years from baseline, scaled by the RMSE score from the age and sex dependent population mean (relative RMSE scores). We show the predictions from the 1D summary model starting from the baseline value (purple stars), our network model (red circles), predictions assuming a static baseline value (blue diamonds), an elastic-net linear model (green squares). (Lower is better). **d)** Relative RMSE scores when the when the baseline value for each health variable is imputed for predictions past 5 years from baseline. We show the predictions from the 1D summary model starting from the imputed value (purple stars), our network model (red circles), and predictions with an elastic-net linear model (green squares).

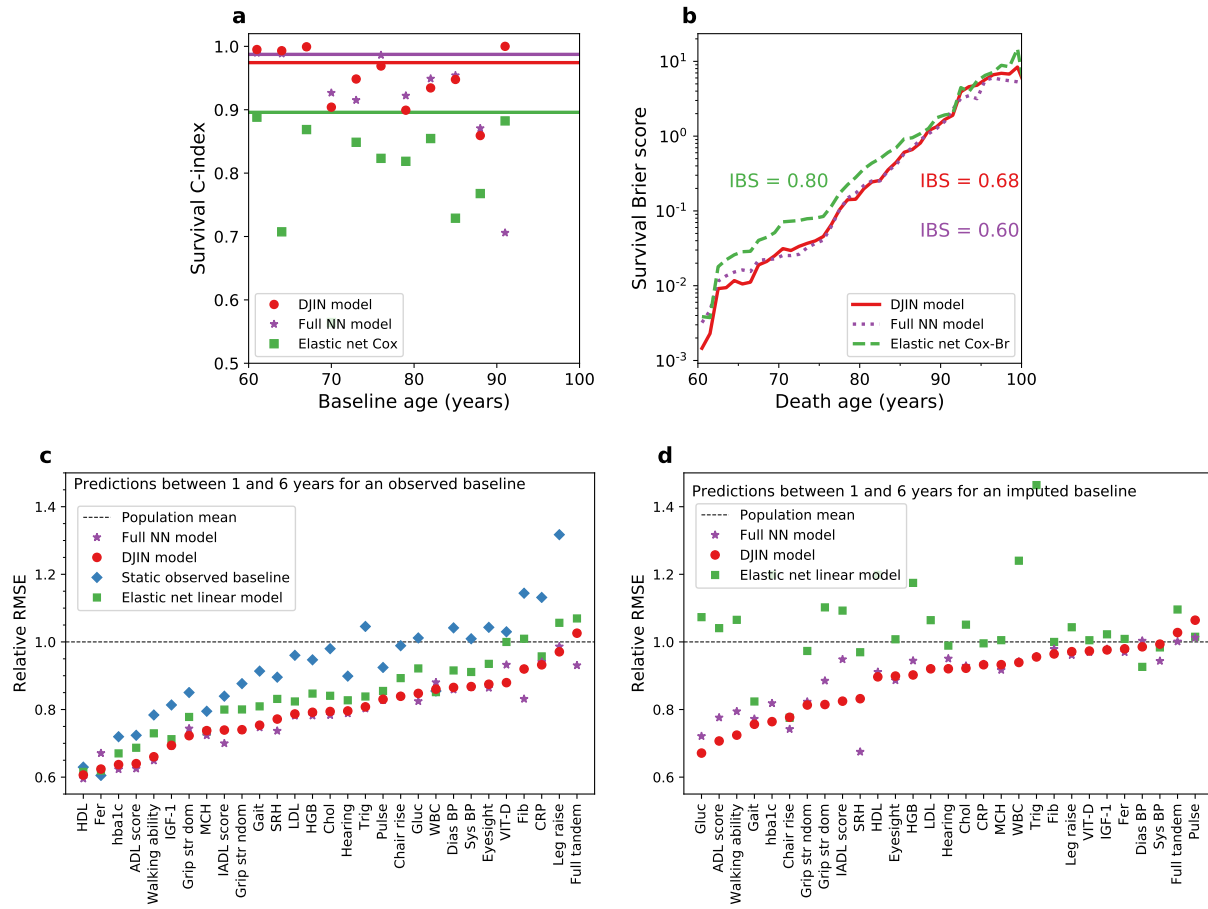


FIG. S11. **Full neural network drift model.** **a)** Time-dependent C-index stratified vs age (points) and for all ages (line). Results are shown for the full neural network model (purple), the DJIN network model shown in the main results (red) and a Elastic net Cox model (green). (Higher scores are better). **b)** Brier scores for the survival function vs death age. Integrated Brier scores (IBS) over the full range of death ages is also shown. (Lower scores are better). **c)** RMSE scores when the baseline value is observed for each health variable for predictions at least 5 years from baseline, scaled by the RMSE score from the age and sex dependent population mean (relative RMSE scores). We show the predictions from the full neural network model starting from the baseline value (purple stars), our network model (red circles), predictions with a static baseline value (blue diamonds), an elastic-net linear model (green squares). (Lower is better). **d)** Relative RMSE scores when the when the baseline value for each health variable is imputed for predictions past 5 years from baseline. We show the predictions from the full neural network model starting from the imputed value (purple stars), our network model (red circles), and predictions with an elastic-net linear model (green squares).

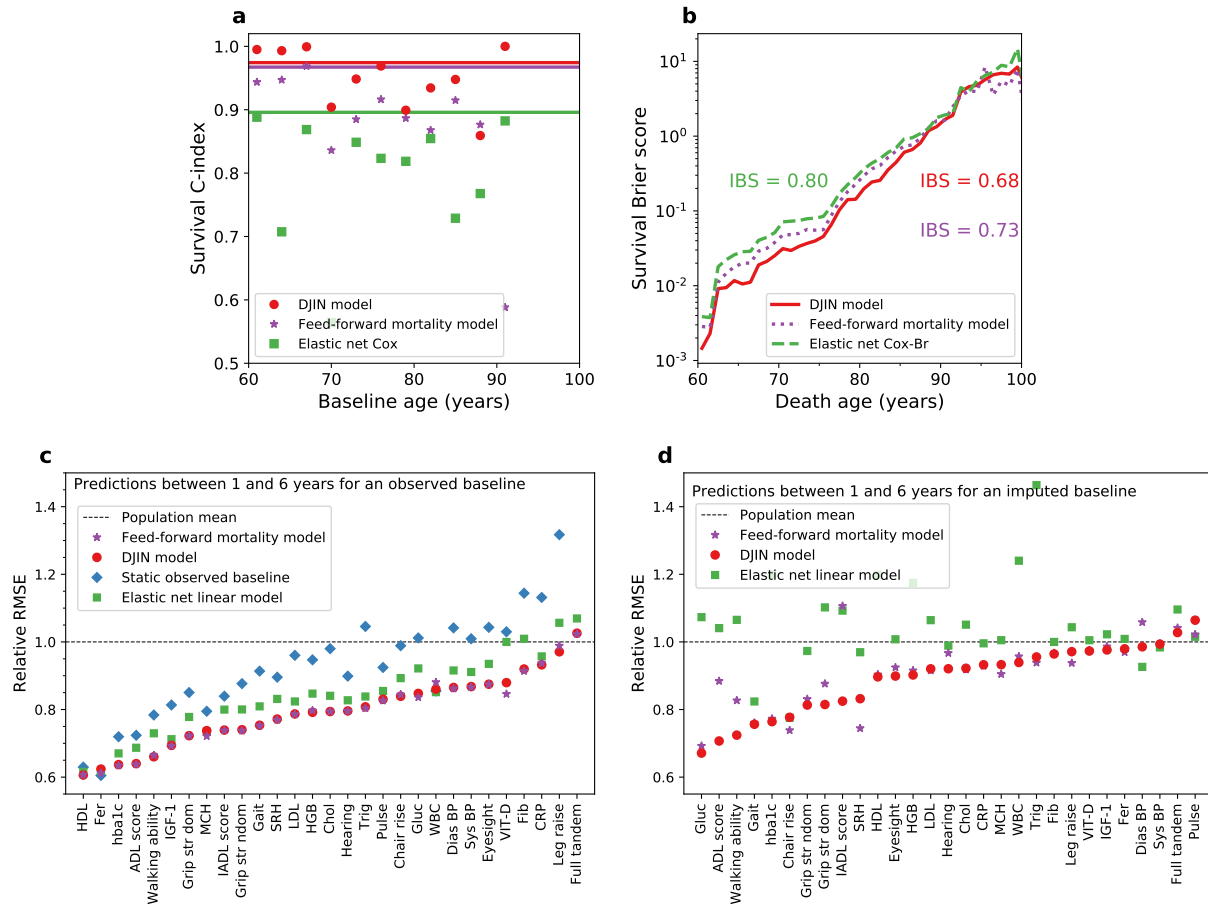


FIG. S12. **Feed-forward mortality rate model.** **a**) Time-dependent C-index stratified vs age (points) and for all ages (line). Results are shown for the feed-mortality mortality rate model (purple), the DJIN network model with a recurrent neural network mortality rate shown in the main results (red) and a Elastic net Cox model (green). (Higher scores are better). **b**) Brier scores for the survival function vs death age. Integrated Brier scores (IBS) over the full range of death ages is also shown. (Lower scores are better). Our DJIN model performs better than the feed-forward mortality model. **c**) RMSE scores when the baseline value is observed for each health variable for predictions at least 5 years from baseline, scaled by the RMSE score from the age and sex dependent population mean (relative RMSE scores). We show the predictions from the feed-forward model starting from the baseline value (purple stars), our DJIN model (red circles), predictions assuming a static baseline value (blue diamonds), an elastic-net linear model (green squares). (Lower is better). **d**) Relative RMSE scores when the when the baseline value for each health variable is imputed for predictions past 5 years from baseline. We show the predictions from the feed-forward mortality model starting from the imputed value (purple stars), our DJIN model (red circles), and predictions with an elastic-net linear model (green squares). For longitudinal predictions, the DJIN model is almost equivalent to the feed-forward mortality model.

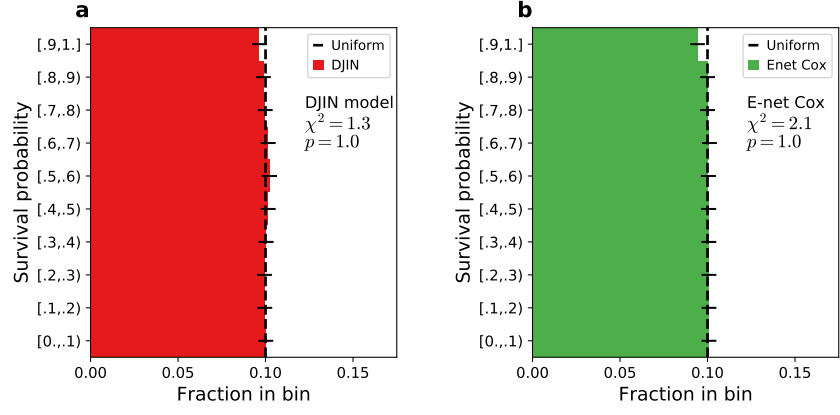


FIG. S13. **D-calibration comparison with elastic-net Cox model.** **a)** D-calibration of survival predictions for the DJIN model. Estimated survival probabilities are expected to be uniformly distributed (dashed black line). We use Pearson's χ^2 test to assess the distribution of survival probabilities finding $\chi^2 = 1.3$ and $p = 1.0$ and an elastic net Cox model. (Higher p-values and smaller χ^2 statistics are better). **b)** D-calibration of survival predictions for the elastic-net Cox model. Estimated survival probabilities are expected to be uniformly distributed (dashed black line). We use Pearson's χ^2 test to assess the distribution of survival probabilities finding $\chi^2 = 2.1$ and $p = 1.0$. Error bars show the standard deviation.